



Detailed Abundances of the Planet-hosting TOI-1173 A/B System: Possible Evidence of Planet Engulfment in a Very Wide Binary

Jhon Yana Galarza^{1,11} , Henrique Reggiani² , Thiago Ferreira³ , Diego Lorenzo-Oliveira⁴ , Joshua D. Simon¹ , Andrew McWilliam¹ , Kevin C. Schlaufman⁵ , Paula Miquelarena^{6,7,8} , Matias Flores Trivigno^{6,7,8} , and Marcelo Jaque Arancibia^{9,10}

¹ The Observatories of the Carnegie Institution for Science, 813 Santa Barbara Street, Pasadena, CA 91101, USA; jyanagalarza@carnegiescience.edu

² Gemini South, Gemini Observatory, NSF's NOIRLab, Casilla 603, La Serena, Chile

³ Department of Astronomy, Yale University, 219 Prospect St., New Haven, CT 06511, USA

⁴ Laboratório Nacional de Astrofísica, Rua Estados Unidos 154, 37504-364, Itajubá - MG, Brazil

⁵ William H. Miller III Department of Physics and Astronomy, Johns Hopkins University, 3400 N Charles St, Baltimore, MD 21218, USA

⁶ Instituto de Ciencias Astronómicas, de la Tierra y del Espacio (ICATE), España Sur 1512, CC 49, 5400 San Juan, Argentina

⁷ Facultad de Ciencias Exactas, Físicas y Naturales, Universidad Nacional de San Juan, San Juan, Argentina

⁸ Consejo Nacional de Investigaciones Científicas y Técnicas (CONICET), Argentina

⁹ Instituto de Investigación Multidisciplinar en Ciencia y Tecnología, Universidad de La Serena, Raúl Bitrán 1305, La Serena, Chile

¹⁰ Departamento de Física y Astronomía, Universidad de La Serena, Av. Cisternas 1200, La Serena, Chile

Received 2024 March 19; revised 2024 July 1; accepted 2024 July 29; published 2024 October 8

Abstract

Over the last decade, studies of large samples of binary systems have identified chemical anomalies and shown that they might be attributed to planet formation or planet engulfment. However, both scenarios have primarily been tested in pairs without known exoplanets. In this work, we explore these scenarios in the newly detected planet-hosting wide binary TOI-1173 A/B (projected separation $\sim 11,400$ au), using high-resolution MAROON-X and ARCES spectra. We determined photospheric stellar parameters both by fitting stellar models and via the spectroscopic equilibrium approach. Both analyses agree and suggest that they are cool main-sequence stars located in the thin disk. A line-by-line differential analysis between the components (B–A) displays an abundance pattern in the condensation temperature plane, where the planet-hosting star TOI-1173 A is enhanced in refractory elements such as iron by more than 0.05 dex. This suggests the engulfment of $\sim 18 M_{\oplus}$ of rocky material in star A. Our hypothesis is supported by the dynamics of the system (detailed in our companion paper), which suggest that the super-Neptune TOI-1173 A *b* might have been delivered to its current short period (~ 7 days) through circularization and von Zeipel–Lidov–Kozai mechanisms, thereby triggering the engulfment of inner rocky exoplanets.

Unified Astronomy Thesaurus concepts: Binary stars (154); Spectroscopy (1558); Stellar abundances (1577); Stellar atmospheres (1584); Fundamental parameters of stars (555); Solar analogs (1941); Exoplanets (498); Hot Neptunes (754)

1. Introduction

It is assumed that the components of a binary system are both co-natal and coeval, meaning they formed from the same parent material at approximately the same time. Consequently, due to this shared origin, they are expected to have a similar chemical composition. Studies of large samples of binary systems using high-resolution ($R = \lambda/\Delta\lambda \geq 50,000$) and high-signal-to-noise-ratio ($\text{SNR} \geq 150 \text{ pixel}^{-1}$) spectra have reported homogeneity between components better than 0.05 dex in $\Delta[\text{Fe}/\text{H}]$ (e.g., Nelson et al. 2021). However, there are also binary systems that do not follow either the co-natal or coeval nature, exhibiting chemical inhomogeneities larger than 0.05 dex (e.g., Hawkins et al. 2020; Nelson et al. 2021; Spina et al. 2021; Yong et al. 2023; Liu et al. 2024). Such inhomogeneities are also found among FGK-type stars when

they are compared with the Sun, in particular in solar twins.¹² Over the last decade, several hypotheses have emerged for understanding the origin of the chemical peculiarities observed in the Sun. One of them was proposed by Gustafsson (2018a, 2018b), suggesting that the chemical makeup of the solar photosphere might have been affected by radiative dust cleansing in the primordial nebula. Adibekyan et al. (2014) proposed that Galactic chemical evolution (GCE) produces trends in the abundances of elements as a function of time, resulting in chemical anomalies when stars of different ages are compared with the Sun. Ramírez et al. (2019) suggested that the chemical abundances of binary systems might be attributed to inhomogeneities in the molecular clouds from which each component forms. This hypothesis also applies to solar twins and the Sun, as they are not formed from the same molecular cloud. Other scenarios include planetary locking and planetary engulfment. Both are the focus of this work, as they have been extensively tested in binary systems (e.g., Ramírez et al. 2011; Tucci Maia et al. 2014; Teske et al. 2016; Saffe et al. 2017; Liu et al. 2021; Spina et al. 2021; Yana Galarza et al. 2021c;

¹¹ Carnegie Fellow.

¹² Solar twins are stars with stellar parameters within $T_{\text{eff}} = 5777 \pm 100$ K, $\log g = 4.44 \pm 0.1$ dex, and $[\text{Fe}/\text{H}] = 0.0 \pm 0.1$ dex (Ramírez et al. 2014).

Flores et al. 2024; Liu et al. 2024; Miquelarena et al. 2024). These scenarios are discussed in detail throughout the paper.

In the context of rocky planet locking, exoplanets can modify star surfaces by sequestering refractory elements during planet formation. As a result, stars that host rocky planets are expected to be deficient in refractory elements. Meléndez et al. (2009) proposed this scenario when they found that the Sun’s refractory elements are deficient compared to the average composition of 11 solar twin stars in the condensation temperature plane.¹³ However, more recent studies, based on disk simulations, suggest that giant exoplanets might also be responsible for the depletion of refractories in the Sun (Booth & Owen 2020; Hühn & Bitsch 2023). In these simulations, the formation of a giant gas planet opens a gap in the protoplanetary disk, trapping the refractory elements and preventing them from falling into the star.

In the planet engulfment scenario, the ingestion of a rocky exoplanet could substantially enhance the refractory elements on the surface of stars. One might also observe an enhancement in the lithium surface abundance, depending on the timing of the engulfment (e.g., Meléndez et al. 2017; Yana Galarza et al. 2021c; Flores et al. 2024).

Over the last two decades, several studies have tested both planet formation and planet engulfment scenarios, mainly using solar-type stars with and without exoplanets. However, as of today, convincing evidence to confirm either of those scenarios is still lacking (e.g., Ramírez et al. 2009; González Hernández et al. 2010; Schuler et al. 2011; Bedell et al. 2018; Yana Galarza et al. 2021a).

Twin-planet-hosting binary systems—namely, components of a pair with similar stellar properties—are likely the key to understanding whether planets can alter the surface of stars. This relies on the assumption that pairs are coeval and co-natal, meaning that any anomalies detected in their components might be associated with the presence of one or more exoplanets. As of today, the chemical abundances of only 37 planet-hosting wide binaries (WBs) have been determined in order to detect planet signatures, namely planet formation or planet engulfment (Ramírez et al. 2011, 2015; Liu et al. 2014, 2018, 2021; Mack et al. 2014; Biazzo et al. 2015; Saffe et al. 2015, 2017, 2019; Teske et al. 2015, 2016; Maia et al. 2019; Jofré et al. 2021; Behmard et al. 2023; Flores et al. 2024). Unfortunately, the results remain inconclusive, due to conflicting findings from different studies. In particular, the planet engulfment scenario is considered less favorable, as pointed out by Behmard et al. (2023), whose findings reveal that the origin of the chemical anomalies is likely primordial. This contradicts the planet engulfment scenario proposed by Spina et al. (2018), Yong et al. (2023), and Liu et al. (2024), aimed at explaining the inhomogeneities observed in WBs, albeit not all stars in their sample harbor exoplanets.

The detection of planet signatures is a challenging task that relies on the precise determination of stellar parameters, such as effective temperature (T_{eff}), metallicity ($[\text{Fe}/\text{H}]$), surface gravity ($\log g$), age, mass, rotation, and magnetic activity. The obtainable precision strongly depends on the quality of the spectra and the selection of a good line list, with well-measured (laboratory measurements) atomic data (e.g., excitation potential and $\log gf$). It has been demonstrated that the analysis

of high-resolution ($\geq 60,000$) and high-SNR (≥ 200) spectra results in better precision not only in stellar parameters, but also when deriving stellar chemical abundances (< 0.05 dex). Additionally, the analysis of dynamical timescales should be considered in planet-hosting WBs to potentially detect planet engulfment triggered by planet migration.

Precision in a chemical analysis significantly increases when employing the differential technique, with a precision as good as ~ 0.01 – 0.02 dex achievable for solar twins (e.g., Meléndez et al. 2009; Nissen 2015; Spina et al. 2016; Bedell et al. 2018; Yana Galarza et al. 2021c), thus opening up the possibility of detecting planet-related signatures on those objects. A caveat is that the achievable precision decreases if there are large differences between the stars. In particular, differences in metallicity and effective temperatures are the largest contributors to a precision decrease (e.g., Reggiani & Meléndez 2017). From a physical perspective, the decrease in precision mostly comes from large enough differences in continuum opacities (which, in a differential abundance analysis, are assumed to be zero). For differences in effective temperatures larger than about 500 K and metallicity differences on the order of 0.15 dex, non-local thermodynamic equilibrium (NLTE) effects are also an important source of differences (which is not our case). From a data analysis perspective, effective temperature differences also contribute to differences during normalization, and continuum placement during line measurements can play an important role in the differential analysis. Any effect that changes the line profile, such as rotation, can influence line measurements and decrease achievable precision. It is also important to highlight that differences in surface gravity must be larger than the differences observed in our pair to have any effect on the achievable precision, as the changes caused in line profiles are mostly observable in saturated and resonant lines, which we avoid in our analysis. Despite these caveats, as we show in Section 3, the differences in the stellar parameters of TOI-1173 A/B are sufficiently small that a differential abundance brings important improvements to the elemental abundance precision. Additional extensive discussions on the benefits of using the differential approach in FGK-type stars are provided in Smiljanic et al. (2007), Ramírez & Allende Prieto (2011), Feltzing & Chiba (2013), Nissen & Gustafsson (2018), and Jofré et al. (2019).

Therefore, in this paper, we adhere to the differential analysis approach to investigate whether the origin of the chemical anomalies detected in the planet-hosting WB TOI-1173 A/B can be attributed to planet signatures. In our companion paper (Yana Galarza et al. 2024), we report the discovery of a super-Neptune in the component TOI-1173 A, thereby expanding the restricted sample of planet-hosting WBs. Our pair represents the second WB system discovered to host planets with separations greater than 10,000 au, following the system HAT-P-4 A, with a separation of $\sim 29,500$ au (Mugrauer et al. 2014; Saffe et al. 2017).

In Section 2.1, we describe the target selection, observations, and data reductions. Section 3 presents the determination of stellar parameters, age, and masses, while Section 4 discusses the inferred chemical composition. In Section 5, we present the discussion of our results. Section 6 provides a summary and conclusions. Finally, the Appendix describes the GCE corrections applied to the binary system, when compared to the Sun.

¹³ In this work, the condensation temperature plane refers to the comparison of the chemical abundances of a star as a function of their condensation temperature.

Table 1

Photometric Parameters and Galactic Orbital and Space Velocities of TOI-1173 A/B

Parameter	TOI-1173A	TOI-1173B
Gaia DR3 G^a	10.804 ± 0.003	11.389 ± 0.003
Gaia DR3 $(B - P)^a$	11.208 ± 0.003	11.856 ± 0.003
Gaia DR3 $(R - P)^a$	10.236 ± 0.004	10.761 ± 0.004
Gaia DR3 parallax ^a	7.566 ± 0.012	7.565 ± 0.016
RUWE ^a	0.839	0.881
RV ^a (km s ⁻¹)	-45.920 ± 0.349	-45.992 ± 0.553
μ_{α}^{*a} (mas yr ⁻¹)	57.786 ± 0.011	57.419 ± 0.015
μ_{δ}^a (mas yr ⁻¹)	-92.392 ± 0.012	-93.021 ± 0.017
2MASS J^b	9.564 ± 0.020	10.043 ± 0.022
2MASS H^b	9.228 ± 0.017	9.598 ± 0.023
2MASS K_s^b	9.134 ± 0.015	9.495 ± 0.020
$E(B - V)^c$	0.010 ± 0.014	
Distance ^d (pc)	$131.810^{+0.193}_{-0.199}$	$131.544^{+0.342}_{-0.252}$
Projected separation	86''735, 11432.592 au	
z_{\max} (kpc)	0.192	0.195
Eccentricity	0.277	0.277
Perigalacticon (kpc)	5.725	5.710
Apogalacticon (kpc)	10.104	10.092
U (km s ⁻¹)	72.282	72.284
V (km s ⁻¹)	39.120	39.559
W (km s ⁻¹)	3.882	4.153
3D velocity difference (km s ⁻¹)	0.516	

Notes. The errors in Gaia magnitudes were adopted from VizieR (Ochsenbein et al. 2000).

^a Gaia Collaboration et al. (2023).

^b Skrutskie et al. (2006).

^c Lallement et al. (2014, 2018).

^d Bailer-Jones et al. (2021).

2. Observations

2.1. Target Selection

The WB system TOI-1173 A/B (Gaia DR3 1686171213716517504 and Gaia DR3 1686170870119133440, respectively) was selected using the color constraints of Yana Galarza et al. (2021b; see their Table 1), originally designed to identify FGK-type stars in the Gaia database (Gaia Collaboration et al. 2023), but now applied to the one million binaries in the catalog of El-Badry et al. (2021). The components of the pair share identical radial velocities (RVs), and their Gaia renormalized unit weight errors (RUWEs; Gaia Collaboration et al. 2023), which is an indicator of multiplicity, are lower than 1 (see Table 1), indicating that the components are not themselves binary systems (Kervella et al. 2022). We corrected the systematic offsets in the Gaia DR3 parallaxes following Lindegren et al. (2021a). The distance was computed by simply inverting the parallax, resulting in ~ 132 pc for both components, in agreement with the distances inferred by Bailer-Jones et al. (2021). The projected separation of the pair was initially estimated as 11,463.25 au by El-Badry et al. (2021). Using the distance from Bailer-Jones et al. (2021), we obtained a similar separation ($\sim 11,400$ au).

We determined Galactic orbits using the GALA¹⁴ code (Price-Whelan 2017; Price-Whelan et al. 2020) and Gaia DR3 astrometry (Gaia Collaboration et al. 2023). In brief, we first transformed the astrometric data and RVs of the pair into galactocentric Cartesian units using ASTROPY (Astropy

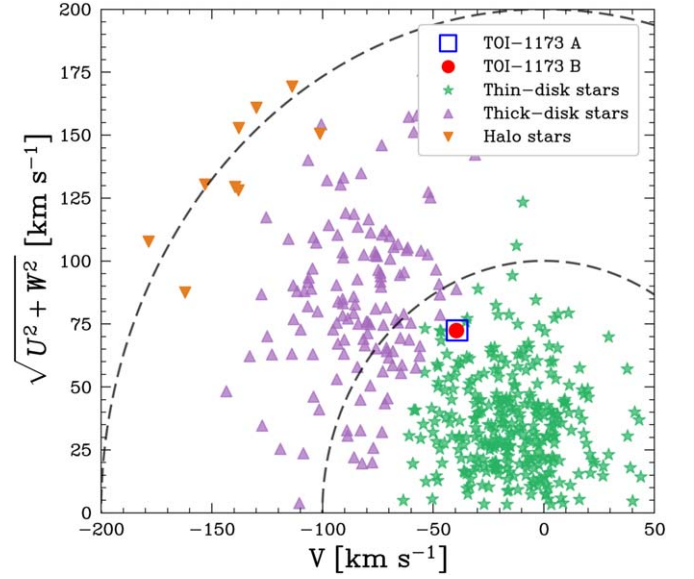


Figure 1. Toomre diagram for the binary system TOI-1173 A/B, indicating that our pair is located in the thin disk. The stars, triangles, and inverted triangle symbols represent stars from the thin disk, thick disk, and halo of the Galaxy, respectively, for context. Data taken from Ramírez et al. (2007).

Collaboration et al. 2022), assuming that the Sun's position and velocity are $x_{\odot} = (-8.3, 0, 0)$ kpc and $v_{\odot} = (-11.1, 244, 7.25)$ km s⁻¹ (Schönrich et al. 2010; Schönrich 2012). Then, we used GALA to carry out the orbital integration with the default potential MILKYWAYPOTENTIAL. This potential is a mass model for the Milky Way consisting of a spherical nucleus and bulge (Hernquist 1990), a Miyamoto–Nagai disk (Miyamoto & Nagai 1975; Bovy 2015), and a spherical Navarro–Frenk–White dark matter halo (Navarro et al. 1996). We used a time step of 1 Myr and integrate for 4 Gyr, corresponding to ~ 20 orbits for each component of the pair.

Our results suggest that both components have similar maximum vertical excursion (z_{\max}), eccentricity, perigalacticon, and apogalacticon values. The Galactic space velocities (U , V , W) place the WB within the thin-disk kinematic distribution on the Toomre diagram (V versus $\sqrt{U^2 + W^2}$; see Figure 1). The Galactic orbits and space velocities are listed in Table 1. We estimated the 3D velocity difference (Δv_{3D}) to be 0.52 km s⁻¹. According to simulations by Kamdar et al. (2019), components with $\Delta v_{3D} < 2$ km s⁻¹ and separations below $\sim 10^7$ au have a high probability of being co-natal. Therefore, given the $\sim 11,400$ au separation and a Δv_{3D} below 1 km s⁻¹, we conclude that TOI-1173 A/B is truly co-natal.

The component A of the binary system hosts a super-Neptune exoplanet. TESS observed TOI-1173 A in nine sectors (7, 14, 15, 21, 22, 41, 47, 48, and 74). As we will describe in Section 2.2, we also obtained MAROON-X spectra for the A component, and using both the transit and RV observations, we infer precise exoplanet parameters, which are listed in Table 2. The mass and radius of TOI-1173 A b yield a density of $\sim 0.195 \pm 0.018$ g cm⁻³, making it the first puffy super-Neptune discovered in a WB system (Yana Galarza et al. 2024). Inflated exoplanets represent a challenge for current models of exoplanet formation. As for hot Jupiters, it is believed that puffy exoplanets might not have formed in situ. Instead, there is a consensus that they might have undergone migration. In Yana Galarza et al. (2024), we discussed the planetary dynamical history in detail, and the migration of this puffy planet

¹⁴ <https://github.com/adrm/gala>

Table 2
Exoplanet Parameters of TOI-1173 A b

Parameter	TOI-1173 A b	Units
Orbital period (P_b)	$7.06466^{+0.00028}_{-0.00029}$	days
Semi-amplitude (K_b)	$9.67^{+0.47}_{-0.46}$	m s^{-1}
Semimajor axis (a_b)	0.0696 ± 0.0014	au
Eccentricity (e_b)	$0.023^{+0.025}_{-0.016}$...
Mass (M_b)	27.4 ± 1.7	M_{\oplus}
Radius (R_b)	9.19 ± 0.18	R_{\oplus}
Density (ρ_b)	$0.195^{+0.018}_{-0.017}$	g cm^{-3}

Note. Data taken from Yana Galarza et al. (2024).

constitutes a crucial component of our planet engulfment hypothesis.

2.2. Spectroscopic Observations

TOI-1173 A and B were observed under the program ID GN-2022A-Q-227 with the high-resolution echelle spectrograph MAROON-X (Seifahrt et al. 2018, 2022) mounted on the 8.1 m Gemini North Telescope of the International Gemini Observatory located in Hawaii. The instrument has a spectral resolution $R \sim 85,000$ and possesses two optical–near-IR channels, with wavelength coverage of 500–670 nm and 650–900 nm for the blue and red channels, respectively. We obtained 10 spectra for TOI-1173 A, three for TOI-1173 B, and one for the Sun. The latter was acquired through the reflected light of the Vesta asteroid. The data reduction was performed by the MAROON-X instrument team using a custom PYTHON3 pipeline that provides optimally extracted and wavelength-calibrated 1D spectra. The RVs were calculated using the SpEctrum Radial Velocity AnaLyser (Zechmeister et al. 2018) pipeline, which creates high-SNR templates by coadding the observed spectra. The templates are then shifted for RV and compared to each individual observation, employing least-squares fitting.

We also obtained spectra for the pair using ARCÉS on the 3.5 m telescope at Apache Point Observatory. A solar spectrum was taken by observing the sky during twilight. Calibration frames, such as biases and flats, were taken in the afternoon of the observations. All observations were conducted in 2023 May. The ARCÉS spectrograph provides spectra with a resolution of $R = 31,500$, covering the entire visible wavelength range from 320 to 1000 nm. The reduction of the ARCÉS data was done via the CERES¹⁵ package. It conducts bias subtraction (via a master bias, calculated as the median value of a series of bias frames observed in the afternoon). Orders are traced with a master flat (calculated as the median value for a series of flats taken in the afternoon calibrations). The master flat, which combines the blue and red channels, is also used for flat-field correction of the science frames. Wavelength calibration relies on a ThAr lamp exposure taken immediately after the science frames. For more details on the ARCÉS data reduction with CERES, we refer the reader to Brahm et al. (2017).

2.3. Data Treatment

We used the ISPEC¹⁶ (Blanco-Cuaresma et al. 2014; Blanco-Cuaresma 2019) tool to carry out radial/barycentric velocity

correction only for the ARCÉS spectra. For the MAROON-X spectra, we employed the RV provided by the MAROON-X instrument team. Once the spectra were shifted to the rest frame, we normalized each individual spectrum with the CONTINUUM task in IRAF¹⁷ by fitting the spectra preferably with third-degree spline functions in the blue orders and low-order polynomials in the red orders. The coaddition of the spectra is done after normalization, using the IRAF SCOMBINE task. It resamples each spectrum and combines them using the average values, therefore increasing the achievable SNR as well. The resulting MAROON-X spectra have SNRs of ~ 540 , ~ 300 , and $\sim 200 \text{ pixel}^{-1}$ at ~ 630 nm for the Sun, TOI-1173 A, and TOI-1173 B, respectively. For the combined ARCÉS spectra, the SNR is 140 pixel^{-1} for the A component and 150 pixel^{-1} for the B component, both at ~ 665 nm.

3. Fundamental Parameters

3.1. Equivalent Widths and Stellar Parameters

We measured the equivalent widths (EWs) of stellar absorption lines by fitting Gaussians to the line profiles using the KAPTEYN¹⁸ kmpfit package (Terlouw & Vogelaar 2016). The line-by-line measurements were carried out by carefully choosing local pseudo-continuum regions of 6 \AA , with the line of interest located at the center. This procedure was performed separately for components A and B, with the Sun as the reference star, and then for component B, with A as the reference. The line list used in this work is an updated version of the line list first presented by Meléndez et al. (2014) and includes information about excitation potentials, oscillator strengths, and laboratory $\log g f$ values. We include hyperfine structure and isotopic contributions from McWilliam (1998), Prochaska & McWilliam (2000), Prochaska et al. (2000), Klose et al. (2002), Cohen et al. (2003), Blackwell-Whitehead et al. (2005a, 2005b), Lawler et al. (2014), and from the Kurucz¹⁹ line lists. To avoid saturation effects, only iron lines with measured $EW < 130 \text{ m\AA}$ were used in the determination of stellar parameters.

The spectroscopic stellar parameters—namely, the effective temperature (T_{eff}), surface gravity ($\log g$), metallicity ($[\text{Fe}/\text{H}]$), and microturbulent velocity (v_t)—are determined via spectroscopic equilibrium, satisfying three conditions: (i) the excitation potential equilibrium to get the T_{eff} ; (ii) ionization equilibrium (the same iron abundance from two ionization stages) to get the $\log g$; and (iii) the nondependence of the differential abundance and the reduced EW ($\log(EW/\lambda)$) to get the v_t . The spectroscopic equilibrium is based on measurements of iron abundances (Fe I and Fe II). In a line-by-line differential analysis, the iron abundance is measured relative to a reference star, usually the Sun. This technique minimizes the impact of model atmospheres as well as errors in laboratory atomic data (e.g., oscillator strengths), since they cancel out in each line calculation. Precision is maximized when both the reference star and the target star are twins. Using solar twins, this method typically achieves a precision of about 10 K in T_{eff} , 0.01 dex in

¹⁵ <https://github.com/rabrahm/ceres>

¹⁶ <https://www.blancocuaresma.com/s/ispec>

¹⁷ IRAF is distributed by the National Optical Astronomical Observatories, which is operated by the Association of Universities for Research in Astronomy, Inc., under a cooperative agreement with the National Science Foundation.

¹⁸ <https://www.astro.rug.nl/software/kapteyn/index.html>

¹⁹ <http://kurucz.harvard.edu/linelists.html>

Table 3
Stellar Parameters of TOI-1173 A/B

ID	T_{eff} (K)	$\log g$ (dex)	[Fe/H] (dex)	v_t (km s ⁻¹)	T_{eff}^a (K)	$\log g^b$ (dex)
q^2 —the Sun as reference						
TOI-1173 A (A–Sun)	5300 ± 9	4.330 ± 0.022	0.117 ± 0.010	0.67 ± 0.03	5367 ± 50	4.423 ± 0.022
TOI-1173 B (B–Sun)	4966 ± 20	4.280 ± 0.022	0.074 ± 0.016	0.40 ± 0.11	5068 ± 43	4.477 ± 0.023
XIRU—the Sun as reference						
TOI-1173 A (A–Sun)	5315 ± 9	4.439 ± 0.052	0.126 ± 0.010	0.77 ± 0.02	5369 ± 51	4.419 ± 0.022
TOI-1173 B (B–Sun)	4995 ± 15	4.451 ± 0.107	0.107 ± 0.020	0.59 ± 0.03	5075 ± 43	4.480 ± 0.022
ISOCHRONES						
TOI-1173 A (A–Sun)	5350 ± 34	4.450 ± 0.020	0.139 ± 0.065	1.11 ± 0.01	5370 ± 50	4.444 ± 0.024
TOI-1173 B (B–Sun)	5047 ± 34	4.530 ± 0.030	0.114 ± 0.069	1.09 ± 0.01	5078 ± 43	4.520 ± 0.025
Differential approach between components using A as reference						
TOI-1173 B (B–A) ^c	5054 ± 8	4.490 ± 0.020	−0.062 ± 0.007	0.99 ± 0.03	Reference star A from ISOCHRONES	
TOI-1173 B (B–A) ^d	4983 ± 8	4.390 ± 0.022	−0.050 ± 0.006	0.55 ± 0.04	Reference star A from XIRU	

Notes.

^a Photometric effective temperature estimated with COLTE (Casagrande et al. 2021).

^b Trigonometric surface gravity calculated following Yana Galarza et al. (2021b).

^c Stellar parameters of B determined using q^2 (Ramírez et al. 2014).

^d Stellar parameters of B determined using XIRU (Alencastro Puls 2023). (B–A) refers to the stellar parameters of the B component relative to the A component.

$\log g$, and 0.01 dex in [Fe/H] (e.g., Ramírez et al. 2014; Bedell et al. 2018; Yana Galarza et al. 2021b).

In line with our previous works, we utilized the automatic Python code Qoyllur-quipu²⁰ (q^2) to determine the stellar parameters through spectroscopic equilibrium. A detailed explanation of q^2 's functionality and performance can be found in Ramírez et al. (2014). We configured q^2 to employ the Kurucz ODFNEW model atmospheres (Castelli & Kurucz 2003) and the 2019 LTE code MOOG (Snedden 1973). The stellar parameters of the pair relative to the Sun and to each other are reported in Table 3. As a sanity check, we estimated photometric T_{eff} using the color– T_{eff} routine COLTE,²¹ which uses Gaia and Two Micron All Sky Survey (2MASS) photometry in the infrared flux method (IRFM) to establish color–effective temperature relations sensitive to [Fe/H] and $\log g$. The IRFM and the routine are well described in Casagrande et al. (2021). Additionally, we also computed $\log g$ through the trigonometric parallax method, as it is a crucial input parameter in the isochrone-fitting method for inferring ages. The trigonometric $\log g$ is calculated using Equation (3) from Yana Galarza et al. (2021b), with Gaia DR3 parallaxes, Johnson V magnitudes (Kharchenko 2001) corrected for reddening using $E(B - V) = 0.01$ (Lallement et al. 2018), bolometric corrections from Meléndez et al. (2006), and stellar masses from isochrone fitting (see Section 3.2).

Table 3 shows an agreement between the photometric and spectroscopic T_{eff} for the A component, but not for the B component, where the difference is ~ 100 K. There is a notable difference between the trigonometric and spectroscopic $\log g$ for both stars, with a deviation of 0.093 dex for star A and 0.197 dex for star B. Such disparities in estimating stellar parameters are not surprising, as the spectroscopic method, especially ionization equilibrium, relies on different physical

assumptions, the quality of the spectra (high SNR and R), and the number of reliable Fe I and Fe II lines with accurate EW measurements.

In our analysis, although the MAROON-X spectra are of high quality, there are only between 10 and 11 clean Fe II lines for each component. This limitation could potentially affect the ionization equilibrium, resulting in incorrect $\log g$ values. On the other hand, as mentioned earlier, the differential analysis technique is more accurate when the reference star is similar to the target star (e.g., Reggiani & Meléndez 2017). This is not the case for our binary system, so the continuum and model atmosphere could influence the excitation/ionization balance of iron lines. It is known that in cool stars, particularly K-type stars, finding the continuum below 500 nm is challenging. To minimize the impact of continuum normalization on the B component, which is the cooler star, we normalized only orders with wavelengths greater than 500 nm. Additionally, we determined the stellar parameters using absolute iron abundances; however, we found similar deviations in $\log g$.

In their study, Delgado Mena et al. (2017) analyzed a sample of FGK stars from the HARPS GTO program and observed significant discrepancies between spectroscopic and trigonometric $\log g$ values. They found an average difference of -0.22 (± 0.10) dex for cool stars ($T_{\text{eff}} < 5200$ K) and 0.21 (± 0.13) dex for hot stars ($T_{\text{eff}} > 6100$ K), as shown in their Figure 2. To address this issue, the authors applied corrections based on linear fits to the difference in $\log g$ versus T_{eff} . The corrected results were more realistic and, as emphasized by the authors, aligned with isochrones in the Kiel diagram ($\log g$ versus T_{eff}). Following Delgado Mena et al. (2017), and assuming that the trigonometric $\log g$ represents the more realistic value for cool stars, we run q^2 by fixing the trigonometric $\log g$ value. Nonetheless, we found significant trends in the excitation balance, reduced EW, and differences between iron abundances inferred from Fe I and Fe II. Thus, the spectroscopic equilibrium cannot be satisfied in any way.

²⁰ <https://github.com/astroChasqui/q2>

²¹ <https://github.com/casaluca/colte>

The origin of the discrepancies between trigonometric and spectroscopic surface gravities is still unknown. Bensby et al. (2014) studied the impact of NLTE effects on Fe I for stars with T_{eff} between 4600 and 6800 K and reported significant changes in the derived $\log g$ for stars with $T_{\text{eff}} > 6000$ K when NLTE effects are included (see their Figure 6). No significant dependence of the surface gravity on the NLTE correction was found for cooler stars ($T_{\text{eff}} < 5500$ K), indicating that NLTE is unlikely to be the origin of the disagreement between the spectroscopic and trigonometric $\log g$ in TOI-1173 A/B. These discrepancies are not new. They have already been reported in other studies (e.g., Mortier et al. 2013; Bensby et al. 2014; Delgado Mena et al. 2014) as a trend of $\log g_{\text{spec}} - \log g_{\text{trig}}$ versus effective temperature, even when $\log g$ is estimated from photometric light curves (see Figure 1 in Tsantaki et al. 2014).

Delving deeper in our analysis, we used the code XIRU²² (Alencastro Puls 2023) to investigate inconsistencies between trigonometric and spectroscopic $\log g$. Similar to q^2 , XIRU is also a Python code written to determine stellar parameters through the spectroscopic equilibrium using MOOG and the Kurucz ODFNEW model atmosphere. However, the methodology is different, as XIRU uses an implementation based on Broyden’s method (Broyden 1965), widely used to solve systems of nonlinear equations by iteratively updating a Jacobian matrix to achieve convergence. As seen in Table 3, the stellar parameters obtained with XIRU are similar to those from q^2 , except for $\log g$, which more closely aligns with the trigonometric values. However, the spectroscopic T_{eff} values are slightly underestimated compared to the photometric T_{eff} . XIRU provides better $\log g$ values than q^2 for cool stars, and the underestimation in $\log g$ computed with q^2 remains unclear.

We also employed the ISOCHRONES package²³ (Morton 2015) to estimate the stellar parameters for the pair. In brief, the ISOCHRONES package fits MESA Isochrones and Stellar Tracks (MIST; Paxton et al. 2011, 2013, 2015, 2018, 2019; Choi et al. 2016; Dotter 2016) using MULTINEST²⁴ (Feroz & Hobson 2008; Feroz et al. 2009, 2019) via PYMULTINEST (Buchner et al. 2014). We fitted the Gaia DR3 G-band magnitude (Arenou et al. 2018; Evans et al. 2018; Hambly et al. 2018; Fabricius et al. 2021; Gaia Collaboration et al. 2021; Lindegren et al. 2021a, 2021b; Torra et al. 2021) and the J , H , and K_s bands from the 2MASS All-Sky Point Source Catalog (Skrutskie et al. 2006). Additionally, we include the Gaia DR3 parallaxes of our targets. The extinction A_V was inferred based on 3D maps of extinction in the solar neighborhood from the Structuring by Inversion the Local Interstellar Medium²⁵ program (Lallement et al. 2014, 2018; Capitanio et al. 2017) and the spectroscopically informed metallicity in our prior (within $[\text{Fe}/\text{H}] = \pm 0.1$ dex). For more details on our methodology, we refer the reader to Reggiani et al. (2022). The resulting stellar parameters are in excellent agreement with the photometric and trigonometric values, with an average difference in T_{eff} and $\log g$ of only 26 K and 0.01 dex, respectively.

Among the three methods discussed above, XIRU and ISOCHRONES provide consistent $\log g$ values with the trigonometric $\log g$. Therefore, we will discuss both methods

in the following sections and how this affects the chemical abundance determinations of the pair.

For the differential approach between components, which allows us to maximize precision in stellar parameters, we chose the A component as the reference star, because it is brighter and has a higher-SNR spectrum. We used q^2 to determine the stellar parameters of component B relative to A (i.e., (B–A)), first using the stellar parameters of A estimated with XIRU, then employing ISOCHRONES. The results are listed in the last two rows of Table 3. Figures 2 and 3 show that the spectroscopic equilibrium for the B component relative to A is satisfied.

3.2. Ages, Masses, and Radii

As an output of the ISOCHRONES fitting described above, we also computed stellar fundamental parameters (namely, masses, ages, luminosities, and radii). We obtained masses of $M = 0.90^{+0.02}_{-0.02} M_{\odot}$ for star A and $M = 0.83^{+0.02}_{-0.02} M_{\odot}$ for star B. The inferred ages were $\tau = 9.3^{+1.4}_{-1.5}$ and $\tau = 8.3^{+3.0}_{-3.0}$ Gyr, for components A and B, respectively.

Alternatively, we derived masses, ages, and radii through another Bayesian approach anchored on a different set of structural models—the Yonsei–Yale evolutionary tracks (Yi et al. 2001; Demarque et al. 2004). This method is similar to the one employed in Grieves et al. (2018) and Lorenzo-Oliveira et al. (2019). In brief, considering the input parameters and their respective errors (T_{eff} , $[\text{Fe}/\text{H}]$, $[\alpha/\text{Fe}]$, $\log g$, Gaia parallaxes, and G , G_{BP} , and G_{RP} magnitudes), the posterior distribution functions were derived from a proper likelihood marginalization along all possible evolutionary steps. During this task, the likelihood was weighted by its respective mass (the Salpeter 1955 mass function) and metallicity (Casagrande 2018) priors. Finally, the desired evolutionary parameter’s median (50th percentile) and $\pm 1\sigma$ intervals (16th to 84th percentiles) were obtained from their respective posterior cumulative distributions. The ages estimated for the A and B components are $\tau = 8.7^{+2.0}_{-1.9}$ Gyr and $\tau = 8.6^{+3.1}_{-3.5}$ Gyr, respectively. The mass inferred for star A is $0.911^{+0.028}_{-0.030} M_{\odot}$ and for star B is $0.839^{+0.033}_{-0.036} M_{\odot}$.

Even though the two inferences use slightly different methodologies and different isochrone tracks were derived from different models, both methods provide consistent ages and masses within the errors. The ages of our pair confirm that they are truly coeval stars, i.e., they were formed at approximately at the same time, although with different masses. The adopted ages and masses used in this work are listed in Table 4.

4. Chemical Composition

4.1. Abundance Differences between Components (B–A)

The best laboratories for testing the star–planet connection are binary systems, particularly when one component hosts an exoplanet while the other does not. If the components of planet-hosting binary systems are co-natal and coeval, possible departures in the differential abundance between components could be attributed to planet signatures. The binary pair TOI 1173 A/B is then the perfect test bed for this hypothesis, as they are co-natal and coeval, and to the best of our knowledge only TOI-1173 A hosts an exoplanet (see Yana Galarza et al. 2024). Therefore, we performed a differential analysis on TOI 1173 A/B, using the A component as the reference star (B–A),

²² <https://github.com/arthur-puls/xiru>

²³ <https://github.com/timothydmorton/isochrones>

²⁴ <https://ccpforge.cse.rl.ac.uk/gf/project/multinest/>

²⁵ <https://stilism.obspm.fr/>

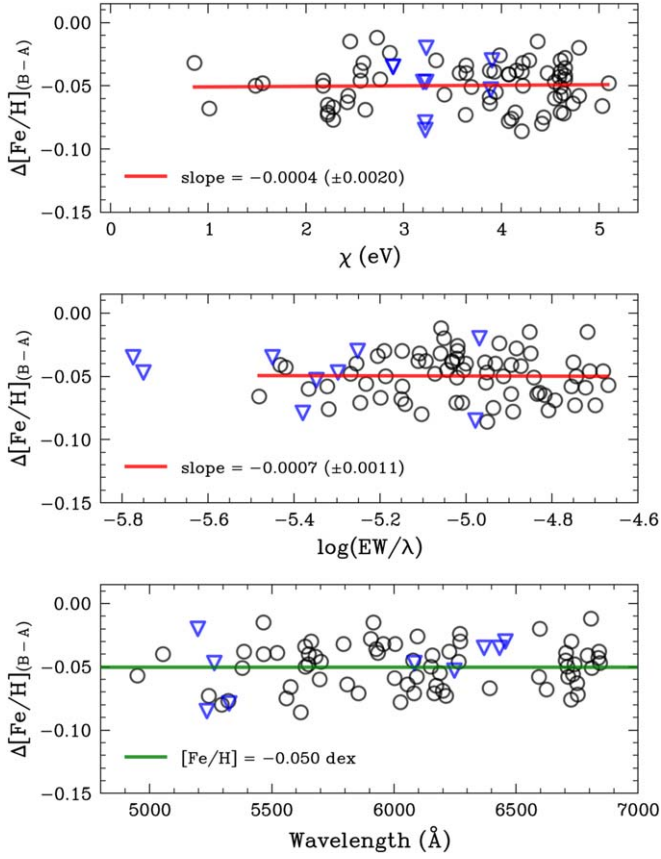


Figure 2. Iron abundances measured in the spectrum of TOI-1173 B relative to TOI-1173 A as a function of excitation potential (top panel), reduced EW (middle panel), and wavelength (bottom panel). The black open circles and blue triangles correspond to Fe I and Fe II lines, respectively. In the top and middle panels, the red solid lines are linear fits to the Fe I abundances. In the lower panel, the green solid line is at the average $\Delta[\text{Fe}/\text{H}]$ value. The adopted stellar parameters for the reference star TOI-1173 A were inferred using XIRU.

since the two stars are more similar to each other than either is to the Sun.

The chemical abundances were estimated from an EW analysis, using a procedure similar to that for Fe I and Fe II, involving fitting Gaussians and selecting local continua in the normalized spectra. This process was performed for component B with component A as the reference. We measured high-precision abundances for 19 elements (O I, Na I, Mg I, Al I, Si I, K I, Sc I, Sc II, Ti I, Ti II, V I, Fe I, Fe II, Co I, Cu I, Zn I, Rb I, Y II, Ba II, Ce II, Nd II, and Eu II). Our line list accounts for hyperfine structure and isotopic splitting for the following elements: Sc I, Sc II, V I, Mn I, Co I, Cu I, Y II, Ba II, and Eu II, from McWilliam (1998), Prochaska & McWilliam (2000), Prochaska et al. (2000), Klose et al. (2002), Cohen et al. (2003), Blackwell-Whitehead et al. (2005a, 2005b), Lawler et al. (2014), and from the Kurucz²⁶ line lists.

We also computed abundances for C I, Ni I, Si I, Ca I, Mn I, Cr I, Cr II, and Ni I, using spectral synthesis with the line list generated from LINEMAKE²⁷ (Placco et al. 2021), updated with more recent laboratory data, when available. The abundance of lithium was also estimated using spectral synthesis and is described in Section 4.2. The choice to employ spectral synthesis instead of EW measurements relies on the fact that

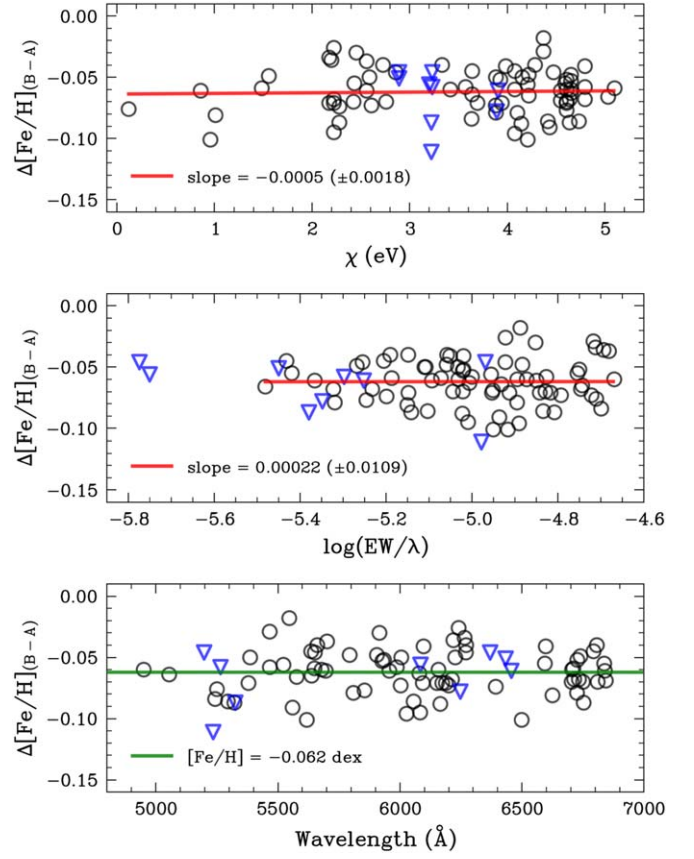


Figure 3. The same as Figure 2, but with the stellar parameters of the reference star TOI-1173 A inferred using ISOCHRONES.

Table 4

Ages, Masses, and Radii of the Components of the Binary System TOI-1173 A/B

ID	Age (Gyr)	Mass (M_{\odot})	Radius (R_{\odot})
Using XIRU-based stellar parameters			
TOI-1173 A	$8.3^{+1.9}_{-1.3}$	$0.910^{+0.013}_{-0.018}$	$0.928^{+0.013}_{-0.013}$
TOI-1173 B	$8.1^{+2.5}_{-1.3}$	$0.838^{+0.013}_{-0.018}$	$0.805^{+0.010}_{-0.013}$
Using ISOCHRONES-based stellar parameters			
TOI-1173 A	$8.7^{+2.0}_{-1.9}$	$0.911^{+0.028}_{-0.030}$	$0.934^{+0.011}_{-0.011}$
TOI-1173 B	$8.6^{+3.1}_{-3.5}$	$0.839^{+0.033}_{-0.036}$	$0.820^{+0.010}_{-0.011}$

Note. All these parameters were inferred through a Bayesian approach that uses the Yonsei–Yale evolutionary models (Yi et al. 2001; Demarque et al. 2004).

these lines are strongly blended, resulting in overestimated EW measurements. To measure nitrogen, we initially determined the carbon abundance from the forbidden [C I] line at 8727 Å and the optical C I 5052 and 5053 Å lines. Subsequently, we employed the average carbon value to calculate the nitrogen abundance from the CN-dominated lines at 7111 and 7113 Å. We validated this procedure using the solar spectrum. Our results for carbon ($A(\text{C}) = 8.400 \pm 0.046$ dex) and nitrogen ($A(\text{N}) = 7.83 \pm 0.07$ dex) in the Sun are in good agreement with those (8.46 and 7.83 dex) estimated by Asplund et al. (2021). The same procedure was applied to determine C I and nitrogen for TOI-1173 A/B. The chemical makeup of B relative to A is listed in Table 5.

²⁶ <http://kurucz.harvard.edu/linelists.html>

²⁷ <https://github.com/vmplacco/linemake>

Table 5
Stellar Abundances for the Wide Binary TOI-1173 A/B

Element	Z	TOI-1173 (B–A) ^a $\Delta[X/H]$ (dex)	Model ^b $\Delta[X/H]_{(B-A)}$ (dex)	TOI-1173 (B–A) ^c $\Delta[X/H]$ (dex)	Model ^d $\Delta[X/H]_{(B-A)}$ (dex)	T_{Cond} (K)
Li ^c	3	0.010 ± 0.100	2.211	0.010 ± 0.100	2.211	1142
C I	6	−0.021 ± 0.011	−0.001	−0.030 ± 0.080	−0.001	40
N I	7	0.020 ± 0.090	−0.000	0.090 ± 0.100	−0.000	40
O I ^f	8	0.030 ± 0.030	−0.022	0.032 ± 0.022	−0.020	180
Na I	11	−0.021 ± 0.010	−0.034	−0.012 ± 0.012	−0.028	958
Mg I	12	−0.081 ± 0.006	−0.070	−0.088 ± 0.006	−0.074	1336
Al I	13	−0.077 ± 0.012	−0.081	−0.081 ± 0.014	−0.084	1653
Si I	14	−0.091 ± 0.013	−0.073	−0.102 ± 0.012	−0.076	1310
S I	16	0.035 ± 0.040	−0.019	0.020 ± 0.050	−0.011	664
K I	19	−0.114 ± 0.057	−0.027	−0.100 ± 0.060	−0.022	1006
Ca I	20	−0.032 ± 0.014	−0.079	−0.025 ± 0.056	−0.082	1517
Sc I	21	−0.034 ± 0.064	−0.065	−0.021 ± 0.049	−0.067	1659
Sc II	21	−0.074 ± 0.011	−0.065	−0.063 ± 0.011	−0.067	1659
Ti I	22	−0.067 ± 0.027	−0.067	−0.058 ± 0.022	−0.070	1582
Ti II	22	−0.097 ± 0.017	−0.067	−0.091 ± 0.018	−0.070	1582
V I	23	−0.031 ± 0.016	−0.089	−0.023 ± 0.014	−0.092	1429
Cr I	24	−0.044 ± 0.014	−0.074	−0.037 ± 0.020	−0.078	1296
Cr II	24	0.011 ± 0.013	−0.074	−0.000 ± 0.030	−0.078	1296
Mn I	25	0.021 ± 0.041	−0.047	0.023 ± 0.050	−0.045	1158
Fe ^g	26	−0.049 ± 0.010	−0.068	−0.058 ± 0.010	−0.072	1334
Co I	27	−0.100 ± 0.010	−0.060	−0.087 ± 0.009	−0.064	1352
Ni I	28	−0.018 ± 0.035	−0.069	−0.023 ± 0.050	−0.073	1353
Cu I	29	−0.073 ± 0.026	−0.041	−0.075 ± 0.025	−0.035	1037
Zn I	30	0.035 ± 0.037	−0.019	0.030 ± 0.030	−0.011	726
Rb I	37	−0.025 ± 0.016	−0.028	−0.020 ± 0.050	−0.021	800
Y II	39	−0.105 ± 0.027	−0.067	−0.102 ± 0.027	−0.069	1659
Ba II	56	−0.121 ± 0.018	−0.064	−0.116 ± 0.018	−0.066	1455
Ce II	58	−0.156 ± 0.025	−0.079	−0.130 ± 0.024	−0.082	1478
Nd II	60	−0.111 ± 0.011	−0.083	−0.093 ± 0.010	−0.086	1602
Eu II	63	−0.050 ± 0.031	−0.076	−0.038 ± 0.026	−0.079	1356

Notes.^a Differential chemical abundances of B relative to A inferred using XIRU-based stellar parameters.^b Model engulfment for abundances from XIRU.^c Differential chemical abundances of B relative to A estimated using ISOCHRONES-based stellar parameters.^d Model engulfment for abundances from ISOCHRONES. The last column is the 50% dust condensation temperature of elements (Lodders 2003).^e NLTE absolute abundances of lithium ($A(\text{Li})_{\text{NLTE}}$), based on the corrections of Lind et al. (2009).^f Oxygen NLTE-corrected abundances using the grades of Ramírez et al. (2007).^g Weighted average of Fe I and Fe II.

Figure 4 shows the differential abundance between components (B–A) as a function of the condensation temperature for abundances inferred using the XIRU-based stellar parameters (upper panel) and ISOCHRONES-based stellar parameters (bottom panel). Both panels display an abundance pattern in which component B is deficient in refractory elements compared to component A. However, both components display a similar abundance pattern in volatile elements. To determine whether the lower iron abundance for star B is due to uncertain differential atmosphere parameters relative to star A, we performed an LTE analysis using the KURUCZ ODFNEW model atmospheres and MOOG. This was applied only to the abundances inferred with the ISOCHRONES, since the abundance pattern slope of this model is less significant. To increase the star B iron abundance (both Fe I and Fe II) by ~ 0.05 dex, thus bringing it into agreement with star A, it was necessary to increase the differential T_{eff} of star B by 80 K and simultaneously increase $\log g$ by 0.17 dex; this corresponds to a 10σ differential temperature change plus an 8σ differential $\log g$ change. Thus, it is not possible to make the iron abundance in star B and star A agree within the uncertainties of the differential atmosphere

parameters, and we conclude that the deficit of Fe, and other refractory elements, in star B relative to star A is real.

It is worth noting that for (B–A), the abundance of Zn at 4722.159 Å was estimated using ARCEN spectra, because the MAROON-X spectra presented artifacts at the Zn transition. Another challenging element to measure was K I. The two strong potassium transitions (7664 and 7698 Å) can be affected by the interstellar medium as well as telluric lines (in particular the 7664 Å), and both transitions are typically highly saturated and with large NLTE departures (Reggiani et al. 2019). Other elements, such as Na I, V I, Y II, Ba II, and particularly chromium, titanium and scandium, were also estimated using ARCEN, and our results are in excellent agreement with our MAROON-X results. In the differential technique, departures from NLTE and GCE effects are minimized, and despite the fact that the components of the pair are not identical twins, the abundance pattern is evident.

4.2. Lithium Abundance

Carlos et al. (2016, 2019), Martos et al. (2023), and Rathsam et al. (2023) have shown that the photospheric ^7Li

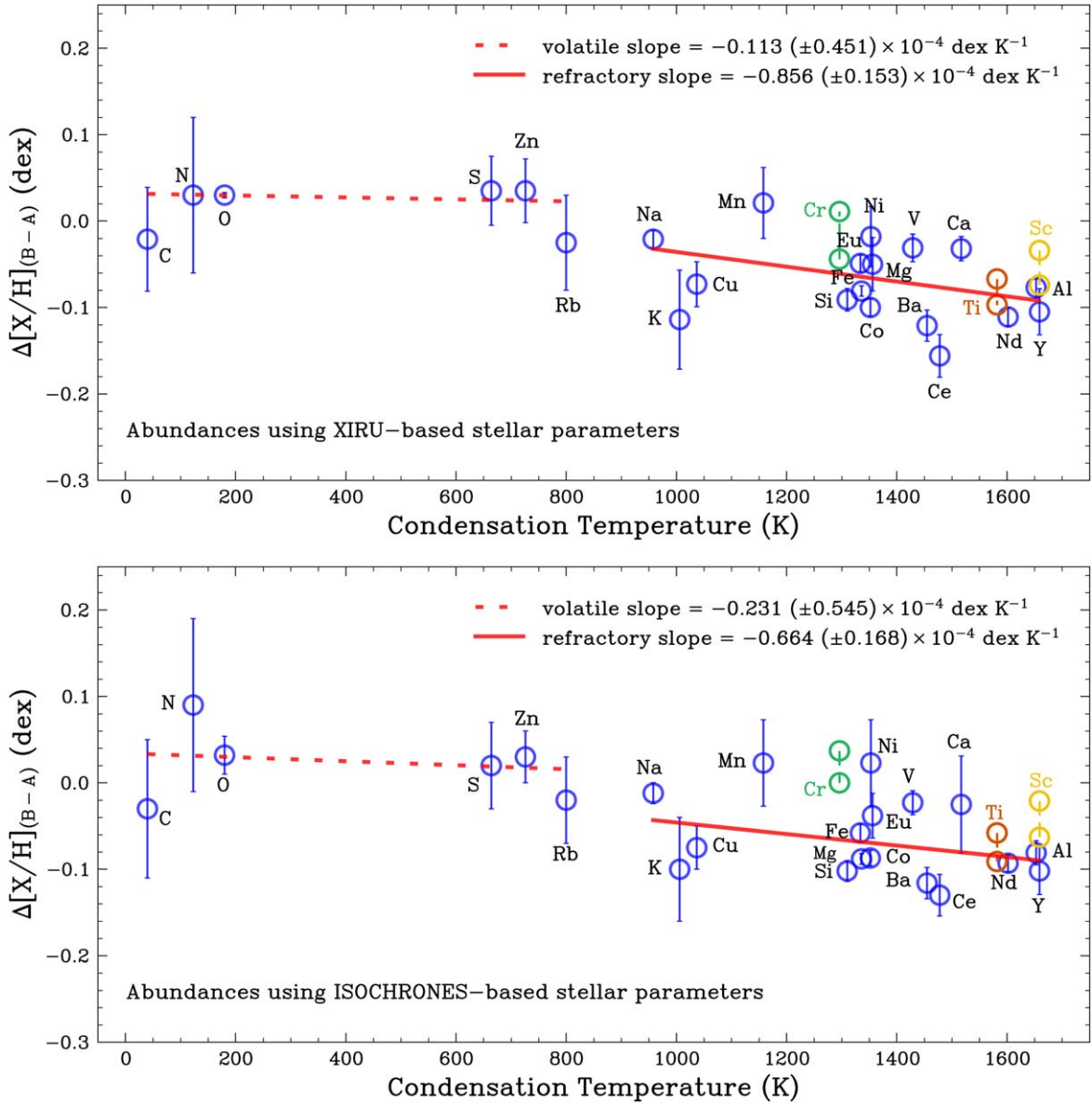


Figure 4. Differential chemical abundances of TOI-1173 B relative to TOI-1173 A as a function of condensation temperature for stellar parameters estimated with XIRU (upper panel) and ISOCHRONES (bottom panel). The linear red solid and red dashed lines are the fits to the refractory ($T_C > 900$ K) and volatile elements ($T_C < 900$ K), respectively. The vertical dashed lines connect two species of the same chemical element (e.g., Cr I and Cr II).

abundance (hereafter, $A(\text{Li})$) in solar-type stars decreases over time. In order to determine $A(\text{Li})$ in our pair, we synthesized the region around the asymmetric 6707.75 Å Li line using the radiative transfer code MOOG, which assumes LTE, with Kurucz model atmospheres. A detailed description of the method can be found in Yana Galarza et al. (2016b) and Martos et al. (2023). In both the MAROON-X and ARCES spectra, we did not detect lithium, but we measured upper limits of $A(\text{Li})_A = 0.040 \pm 0.130$ and $A(\text{Li})_B = 0.010 \pm 0.130$. It can be observed that there is a consensus that both stars are severely depleted in lithium. In addition, the low lithium found in the pair is consistent with similar old ages, as older stars are more lithium-depleted (e.g., see Figure 2 in Rathsam et al. 2023). The $A(\text{Li})$ upper limits were corrected for NLTE departures using the INSPECT database,²⁸ based on the corrections of Lind et al. (2009). The obtained results are

0.150 dex for the A component and 0.160 dex for the B component. These values are in good agreement with the lithium-age anticorrelation reported by Martos et al. (2023).

5. Discussion

5.1. Planet Formation and Engulfment Scenarios

Among the different hypotheses used to explain the chemical anomalies observed in solar-type stars and binary systems, especially in pairs exhibiting chemical anomalies between their components, three scenarios are more explored in the literature: planet engulfment, the formation of rocky planets, and the formation of giant gas planets. In this work, we will discuss these scenarios to explain the observed anomalies in our pair.

During planet formation, both rocky and giant planets can deplete refractory elements in the host star (see Section 1). Since only TOI-1173 A hosts a super-Neptune, we would expect to observe a depletion of refractory elements in the A

²⁸ <http://www.inspect-stars.com/>

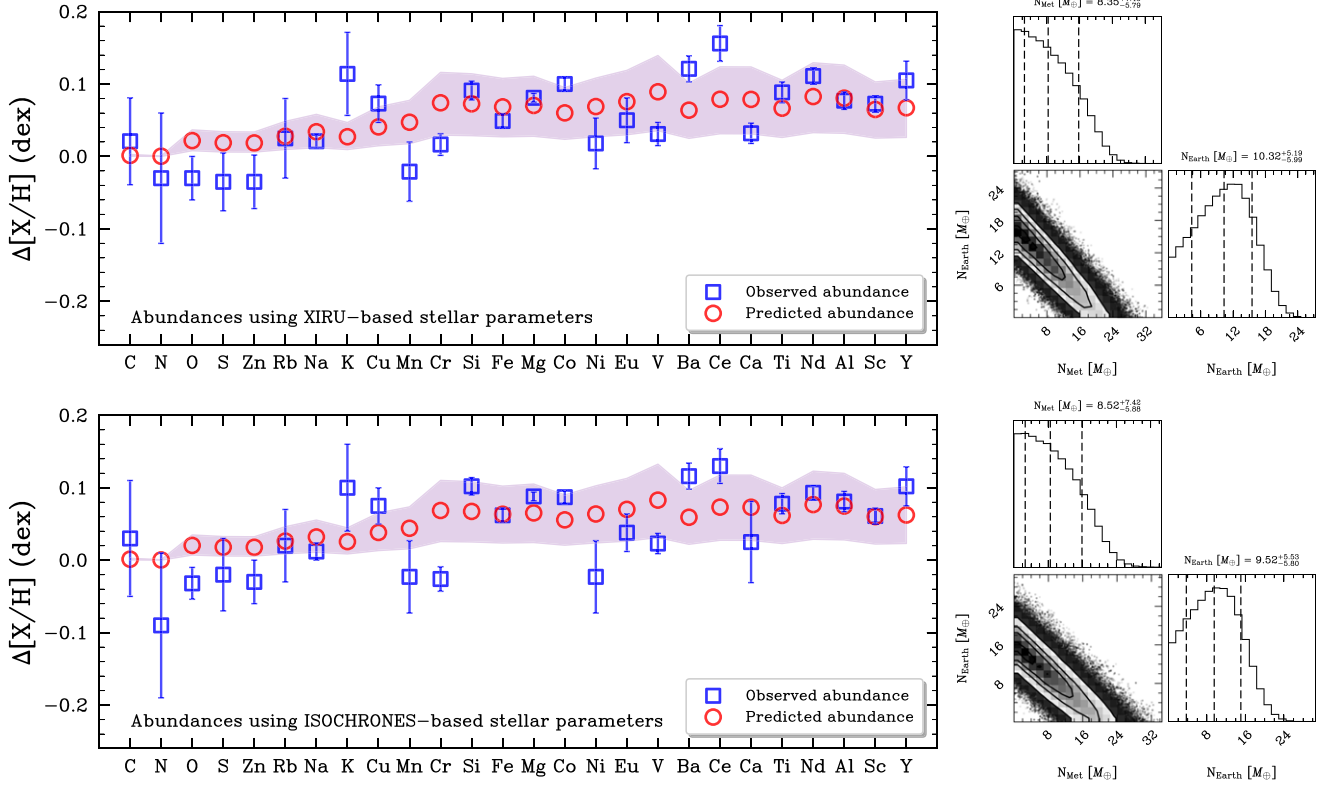


Figure 5. Left panels: differential abundances of TOI-1173 A relative to B as a function of elements in ascending order of condensation temperature. The abundances are calculated using XIRU-based (upper panel) and ISOCHRONES-based (bottom panel) stellar parameters. The observed and model abundances are represented by squares and circles, respectively. The shaded region represents the 1σ posterior probability distribution. Right panels: corner plots showing the results of our Markov Chain Monte Carlo parameter estimation for our planet engulfment model. The dashed lines show the 16% and 84% percentiles for each parameter, thus representing 1σ confidence ranges. The best-fit parameters are also indicated with black dashed lines.

component compared to B. However, the depletion is observed in the star without a known exoplanet, TOI-1173 B. One possible explanation could be that component B may host one or more massive exoplanets (total mass(es) larger than TOI-1173 A *b*), leading to the depletion of its refractory elements at a larger level. To date, we have not detected any transiting planets around TOI-1173 B, and the three MAROON-X spectra we obtained are not yet enough to detect exoplanet signatures via RV variations.

In the engulfment scenario, an enhancement of refractory elements in the form of a positive T_C slope should be observed, followed by, in some cases, an enhancement of the lithium abundance. This scenario is best for explaining the difference between the planet-hosting star A relative to B, i.e., $(A-B)$. To test this hypothesis, we used the TERRA code,²⁹ which predicts the enhancement of volatile and refractory elements that one star may have as a result of the engulfment of a rocky exoplanet (more details in Yana Galarza et al. 2016a).

To reproduce the differential abundance pattern of $(A-B)$, an engulfment of $18.67 M_{\oplus}$ is required for the abundances estimated using XIRU-based stellar parameters. This entails a combination of $\approx 8.35^{+7.45}_{-5.79} M_{\oplus}$ of material with a chondritic composition and $\approx 10.32^{+5.19}_{-5.09} M_{\oplus}$ of Earth-like material (see the upper panels of Figures 5 and 6). For the abundance pattern inferred with ISOCHRONES, the engulfment is $18.04 M_{\oplus}$ ($8.52^{+7.42}_{-5.88} M_{\oplus}$ plus $\approx 9.52^{+5.53}_{-5.80} M_{\oplus}$ of chondritic and Earth-

like material, respectively, are necessary; see the lower panels of Figures 5 and 6). The hypothesis of ingestion of massive exoplanets appears plausible, considering the potential for the formation of such massive exoplanets, as demonstrated by Armstrong et al. (2020). These authors discovered the largest known terrestrial exoplanet, with a mass of $39.1 M_{\oplus}$, which is likely the remnant core of a gas giant that lost its atmosphere through photoevaporation. Interestingly, the host star exhibits parameters similar to those of TOI-1173 A, implying that cores rich in refractory elements might preferentially form around cool, iron-rich stars. However, the detection of more massive terrestrial exoplanets is needed to confirm this.

The engulfment scenario predicts an approximately 2.2 dex enhancement in lithium abundance between components, contradicting the barely detected lithium in both components ($A(\text{Li})_{(A-B)} \sim 0.03$ dex). However, it is worth highlighting that TERRA assumes the engulfment occurred at the star's current age. Therefore, it is reasonable to speculate that the engulfment took place billions of years ago, allowing for the enhanced lithium to burn and reach the current low abundance. This is supported by the planet engulfment simulations of Sevilla et al. (2022), which show that for stars with $0.9 M_{\odot}$ (similar to the mass of TOI-1173 A), the lithium abundance is quickly depleted after accretion, on timescales that are much shorter than the depletion timescales for other chemical elements (~ 1 Gyr versus ~ 10 Gyr).

In Yana Galarza et al. (2024), we also investigated the dynamical timescales of TOI-1173 A in order to explore

²⁹ <https://github.com/ramstojh/terra>

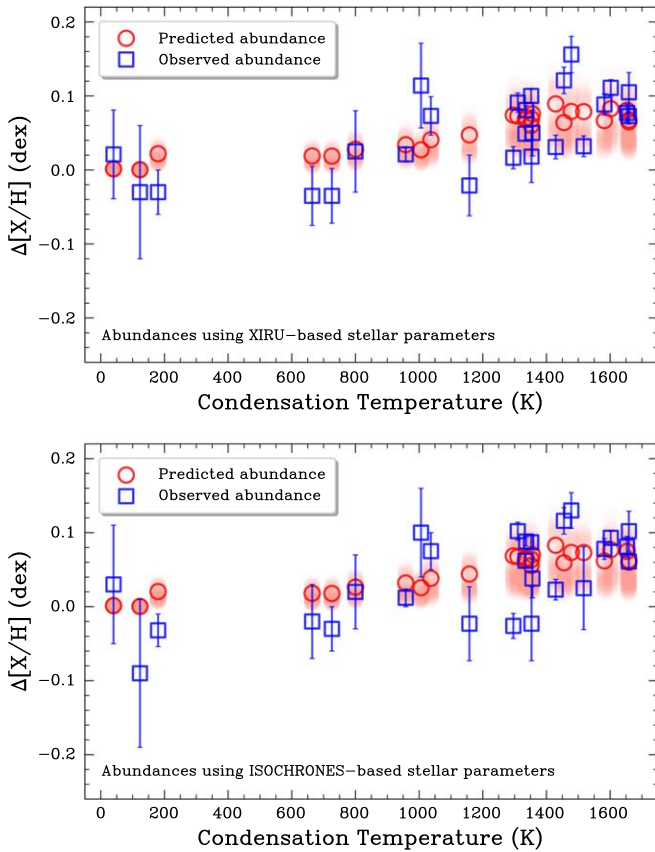


Figure 6. Comparison of the abundances of TOI-1173 A relative to TOI-1173 B (depicted as blue open squares) as a function of the dust condensation temperature for XIRU-based (upper panel) and ISOCHRONES-based (bottom panel) stellar parameters. The predicted abundances are represented as red open circles and were estimated from a planetary engulfment of $\sim 18 M_{\oplus}$ for both models. The blurred red circles show the 1σ posterior probability distribution.

potential interactions between the primary star, its exoplanet, and the companion star, which could have led to the exoplanet’s current orbit. Our results suggest that the time-scales for both tidal circularization and von Zeipel–Lidov–Kozai (vZLK; vasoligation) perturbations range from 10^8 to 10^{11} yr, roughly corresponding to the age of the binary system. We therefore cannot rule out that the super-Neptune TOI-1173 A *b* might have experienced higher eccentricity in the past, which subsequently dampened, leading it to migrate to its current orbit over several billion years.

Several studies have shown that close-in giant planets are formed through high-eccentricity tidal migration (e.g., Rasio & Ford 1996; Wu & Murray 2003; Fabrycky & Tremaine 2007; Raymond et al. 2008; Chambers 2009; Naoz et al. 2012; Mustill et al. 2015; Church et al. 2020; Dong et al. 2021; Rice et al. 2023). Tidal circularization, vZLK perturbations, or both may act as mechanisms for transporting terrestrial planets inward. If a terrestrial planet reaches a semimajor axis of $a \lesssim 0.01$ au, it will fall into the star (Mardling & Lin 2004; Raymond et al. 2008). Therefore, it is possible that the detected super-Neptune orbiting star A might have initially formed with high eccentricity in the outer region of the protoplanetary disk and migrated inward over several billion years, reaching its current semimajor axis (~ 0.07 au), which in turn could have driven interior terrestrial planets below the 0.01 au limit, triggering their engulfment.

5.2. Other Scenarios

Given the projected separation, metallicity, and abundance patterns of TOI-1173 A/B, it is possible to think that the components are not associated and that they are a chance pair of unassociated single field stars moving together. Oh et al. (2018) addressed this possibility for the Kronos/Krios binary system, using a distribution function of single stars in the Milky Way. They found that within 200 pc from the Sun, no stars have small differences between components such as $\Delta\mu_{\alpha}^* < 2$ mas yr $^{-1}$, $\Delta\mu_{\delta} < 2$ mas yr $^{-1}$, and $\Delta v_r < 2$ km s $^{-1}$, meaning that all stars within these values are not comoving by chance. TOI-1173 A/B is within this limit (see Table 1), and along with the 3D velocity difference ($\Delta v_{3D} < 2$ km s $^{-1}$), this reinforces the idea that both components are truly co-natal.

Some works suggest that the chemical abundance differences observed in binary systems might be attributed to primordial inhomogeneities (e.g., Ramírez et al. 2019; Liu et al. 2021; Behrard et al. 2023). More recently, Saffe et al. (2024) determined the chemical composition of the giant–giant binary system HD 138202/CD-30 12303 and found a significant chemical difference between components at the level of 0.08 dex, which is unexpected, as giant stars are sensitive to planet accretion and atomic diffusion effects. After testing those possibilities, they concluded that the chemical differences are attributed to primordial inhomogeneities, as these do not produce condensation temperature trends. Following this, the abundance pattern observed in our pair rules out the scenario of primordial inhomogeneities.

Another possible scenario for explaining the chemical difference in the pair is atomic diffusion. Microscopic diffusion and gravitational settling modify surface chemical abundances of main-sequence stars (e.g., Michaud et al. 1984; Dotter 2016; Liu et al. 2021). In particular, Liu et al. (2021) showed that binary systems with differences between components in $\log g$ and T_{eff} exceeding 0.07 dex and 200 K, respectively, might exhibit non-negligible atomic diffusion effects. As the temperature difference in our pair is ~ 300 K, we explored this possibility by generating stellar evolutionary models using the average metallicity of the pair and ages ranging from 8 to 10 billion years. We adopted the MIST (Dotter 2016) isochrones, based on MESA models, which include mixing via overshooting and atomic diffusion (Choi et al. 2016). Figure 7 depicts the observed abundance difference for three refractory elements (iron, silicon, and magnesium) and one volatile element (oxygen) as a function of surface gravity. The predicted change abundances due to atomic diffusion, estimated from MIST, are represented by the blue shaded region in each panel. It is clear that the observed abundance, represented by triangles (XIRU-based stellar parameters) and squares (ISOCHRONES-based stellar parameters), significantly exceeds the predicted model abundances, in particular for the refractory elements. Similar results are found for other elements. Therefore, we conclude that atomic diffusion does not fully explain the difference in chemical abundances observed between TOI-1173 A and B.

6. Summary and Conclusions

We have determined the precise stellar parameters and chemical composition of the planet-hosting WB TOI-1173 A/B using high-resolution MAROON-X and ARCIS spectroscopy. To infer the stellar parameters, we employed two automatic codes

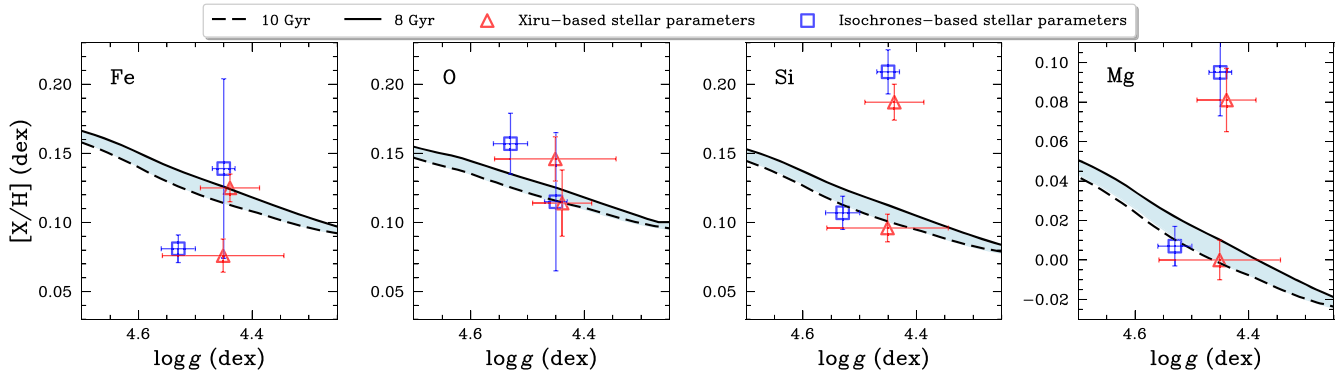


Figure 7. Changing elemental abundances of iron, oxygen, silicon, and magnesium as a function of $\log g$. The blue shaded regions represent the predicted abundance changes for each element due to atomic diffusion, as modeled by MIST (Choi et al. 2016). The models were computed for ages ranging from 8 (solid black lines) to 10 Gyr (dashed black lines). The red triangles and blue squares represent the observed abundances estimated using XIRU-based and ISOCHRONES-based stellar parameters, respectively. Note that the abundances of some elements were vertically shifted to match the model, only to make it clear that atomic diffusion does not explain the abundance difference in the pair.

(q^2 and XIRU) based on spectroscopic equilibrium, using the abundances of Fe I and Fe II to converge to the best solution, with the Sun as the reference star. We also used ISOCHRONES to infer stellar parameters by fitting stellar models. Ages, masses, and radii were inferred via isochrone fitting using Bayesian methods. The resulting fundamental parameters are listed in Tables 3 and 4. Our results indicate that both components are cool and iron-rich stars. The planet-hosting component (TOI-1173 A) is a G9-type star, while component B is a K1.5-type star, according to Gray & Corbally (2009).

We obtained precise chemical abundances for 27 elements, using the Sun as the reference star, denoted as (A-Sun) and (B-Sun). The procedure is explained in Appendix. Figure 8 shows the evolution of the elemental abundance of the stars within 150 pc in the Galactic disk. Both components of the pair follow the GCE trend observed in G-type stars. To compare the components with the Sun, we performed GCE corrections based on fits of elemental abundances and ages. The GCE-corrected abundances of both components were found to resemble those of the Sun in the condensation temperature plane for both volatile and refractory elements (see Figures 9 and 10).

To minimize NLTE and other effects, we then employed the differential technique between components, taking the A component as the reference star. In Figure 4, the differential abundance (B–A) is depicted as a function of condensation temperature, revealing that the B component is depleted in refractory elements. This implies that the component harboring the super-Neptune is abundant in refractory elements, contradicting the planet formation hypothesis. We explored scenarios such as charge captures, primordial inhomogeneities, and atomic diffusion (see Section 5.2). None of these explain the observed abundance difference in the pair, except for atomic diffusion, which has a small contribution. The most promising scenario for explaining the excess of refractory elements observed in star A is the engulfment of a rocky planet (or planets) of $\sim 18 M_{\oplus}$ (see Figures 5 and 6).

To investigate the planet engulfment hypothesis, we explored the dynamical timescales of TOI-1173 A and found that the super-Neptune might have arrived at its observed short period through high-eccentricity migration. The potential mechanisms for the migration are tidal circularization and the vZLK perturbation, as their timescales are comparable to the age of the binary system. Therefore, it is possible that the migration of the super-Neptune TOI-1173 A *b* could have led

to the engulfment of one or more massive rocky planets, enhancing the refractory elements in TOI-1173 A. This scenario might elucidate the observed chemical anomalies of (A–B) in the condensation temperature plane.

Acknowledgments

J.Y.G. acknowledges support from their Carnegie Fellowship. H.R. acknowledges the support from NOIRLab, which is managed by the Association of Universities for Research in Astronomy (AURA) under a cooperative agreement with the National Science Foundation. T.F. acknowledges support from the Yale Graduate School of Arts and Sciences. D.L.-O. acknowledges the support from CNPq (PCI 301612/2024-2).

This work has made use of data collected with the Gemini Telescope. This paper includes data collected by the TESS mission. Funding for the TESS mission is provided by NASA’s Science Mission Directorate. This work has made use of data from the European Space Agency (ESA) mission Gaia (<https://www.cosmos.esa.int/gaia>), processed by the Gaia Data Processing and Analysis Consortium (DPAC; <https://www.cosmos.esa.int/web/gaia/dpac/consortium>). Funding for the DPAC has been provided by national institutions, in particular the institutions participating in the Gaia Multilateral Agreement. This publication makes use of data products from the Two Micron All Sky Survey, which is a joint project of the University of Massachusetts and the Infrared Processing and Analysis Center/California Institute of Technology, funded by the National Aeronautics and Space Administration and the National Science Foundation. This research has made use of the SIMBAD database, operated at CDS, Strasbourg, France (Wenger et al. 2000). This research has made use of the VizieR catalog access tool, CDS, Strasbourg, France (doi:10.26093/cds/vizier). The original description of the VizieR service was published in 2000, A&AS 143, 23 (Ochsenbein et al. 2000).

Facilities: Gemini:Gillett, ARC, Gaia, TESS.

Software: NUMPY (van der Walt et al. 2011), MATPLOTLIB (Hunter 2007), PANDAS (McKinney 2010), ASTROPY (Astropy Collaboration et al. 2022), ASTROQUERY (Ginsburg et al. 2019), IRAF (Tody 1986), ISPEC (Blanco-Cuaresma et al. 2014; Blanco-Cuaresma 2019), KAPTEYN Package (Terlouw & Vogelaar 2016), MOOG (Snedden 1973), q^2 (Ramírez et al. 2014), GALA (Price-Whelan 2017), TERRA (Yana Galarza et al. 2016a), DYNASTY (Speagle 2020), ASTROBASE (Bhatti et al.

2021), XIRU (Alencastro Puls 2023). VOSA (Bayo et al. 2008), SMPLOTLIB (Li 2023).

Appendix Abundance Differences Relative to the Sun

Section 4 describes in detail the calculation of the chemical abundance of the pair using the A component as the reference star. In this section, we apply the same procedure, but we compare each component of the binary system with the Sun. This has some disadvantages, because the A and B components have significantly different temperatures and ages than the Sun. Therefore, GCE corrections and atomic

diffusion must be considered. However, in Section 5.2, it was demonstrated that atomic diffusion does not explain the chemical differences observed in the pair. GCE and NLTE corrections are described below.

The chemical abundances for the pair relative to the Sun, meaning (A-Sun) and (B-Sun), are summarized in Table 6. The $[\alpha/\text{Fe}]$,³⁰ $[\text{Mg}/\text{Fe}]$, and $[\text{Ti}/\text{Fe}]$ values for stars A and B are (0.021, 0.041, 0.012) and (0.003, 0.013, 0.00), respectively, using abundances from ISOCHRONES-based stellar parameters. These values are consistent with the kinematic thin-disk membership of the pair (see Figure 1, and also Figure 7 in Adibekyan et al. 2012, Figure 3 in Fuhrmann et al. 2017, and Figure 23 in Bensby et al. 2014).

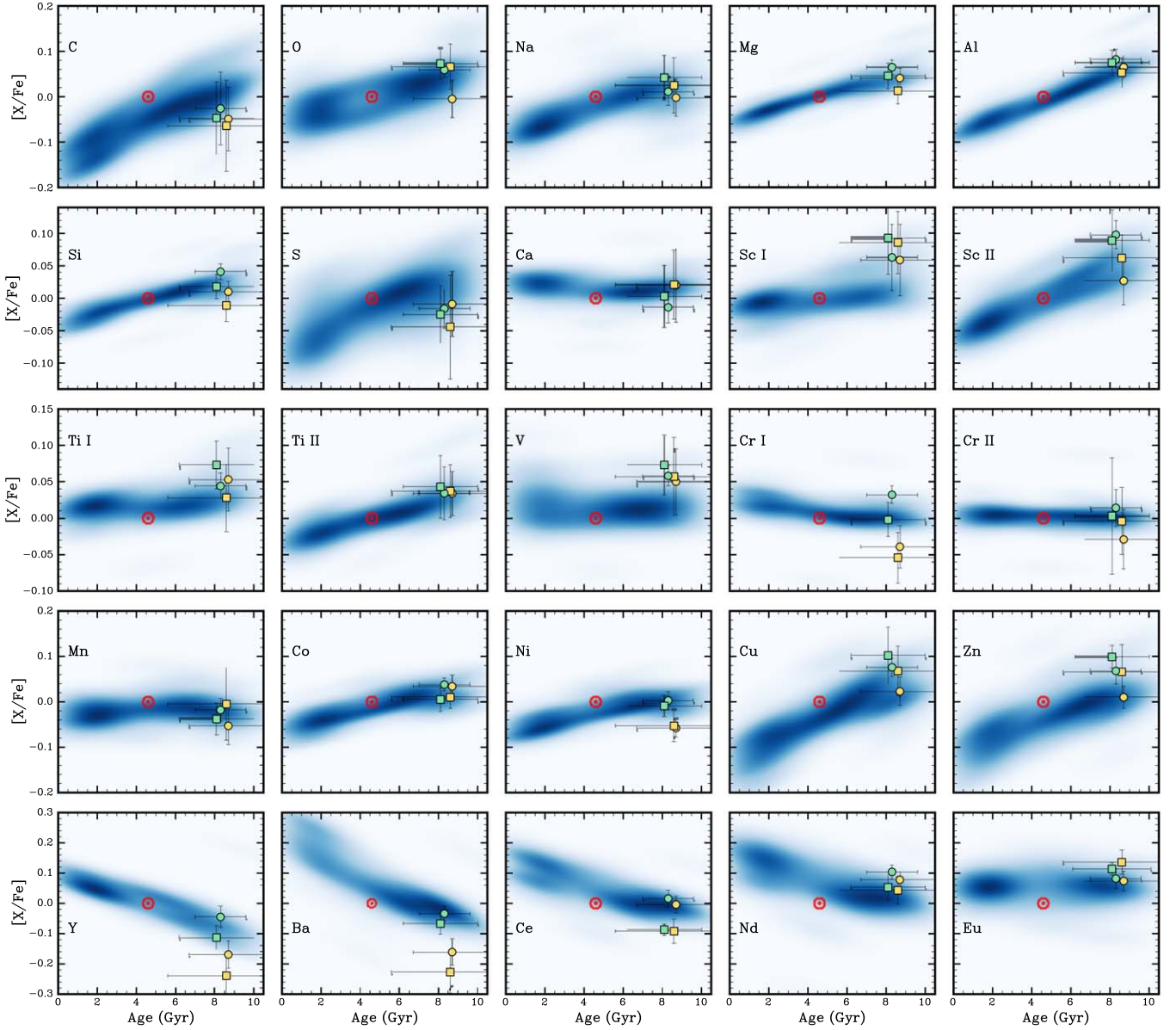


Figure 8. Density plot of elemental abundances of G-type stars (Bedell et al. 2018; Spina et al. 2018; Yana Galarza et al. 2021b) in the thin disk with $5600 \text{ K} \leq T_{\text{eff}} \leq 6000 \text{ K}$ as a function of age. The circle and square symbols represent TOI-1173 A and TOI-1173 B, respectively. The green symbols indicate abundances using XIRU-based stellar parameters, while the yellow symbols use ISOCHRONES-based stellar parameters. For oxygen, the yellow and green symbols represent the NLTE-corrected abundance estimated using the grids of Ramírez et al. (2007). The Sun is plotted as a red solar standard symbol. The ages of the G-type stars were estimated using the Yonsei–Yale evolutionary tracks (Yi et al. 2001), the same models used to infer the adopted age of TOI-1173 A/B.

³⁰ $[\alpha/\text{Fe}] = 1/4 ([\text{Mg}/\text{Fe}] + [\text{Si}/\text{Fe}] + [\text{Ca}/\text{Fe}] + [\text{Ti}/\text{Fe}])$.

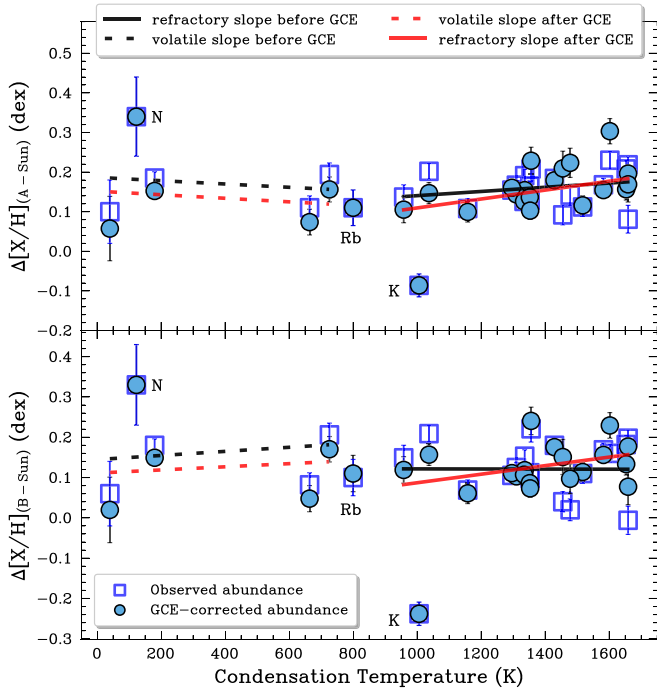


Figure 9. Observed (open squares) and GCE-corrected (filled circles) differential abundances of TOI-1173 A (upper panel) and TOI-1173 B (bottom panel) relative to the Sun as a function of dust condensation temperature. The abundances were estimated using XIRU-based stellar parameters. The green and red solid lines represent the fits to refractory elements ($T_C > 900$ K) before and after applying GCE corrections. The same applies to the dashed lines representing volatile elements ($T_C < 900$ K). The elements N I, Rb I, and K I are not included in the fits.

Similar results are found when using abundances with XIRU-based stellar parameters.

Figure 8 shows a density plot of an updated GCE pattern for 25 elements in thin-disk G stars. The new GCE pattern is based on the solar twin sample of Bedell et al. (2018), but updated with the Inti sample of solar-type stars of Yana Galarza et al. (2021b). The circles and squares represent the chemical compositions of components A and B, while the yellow and green colors indicate the abundances using ISOCHRONES-based and XIRU-based stellar parameters. It is important to mention that as the O I abundances of the new sample of G stars were corrected for NLTE effects using the grids of Ramírez et al. (2007), for consistency, we applied the same NLTE corrections to our pair. Thus, the green symbols in the oxygen trend represent the NLTE correction from this study. From Figure 8, we see that the chemical abundances of both components follow the typical GCE trend of G stars, including the NLTE-corrected abundances. Nonetheless, both components display departures in the C I, Y II, and Ba II elements relative to the GCE trends for G stars when using ISOCHRONES-based stellar parameters. We investigated the possible systematics due to the fact that only one line was available for Y II in MAROON-X spectra, by calculating the same abundances from the ARCEN spectra, and found consistent results. Similar results were found for Ba II using ARCEN. Thus, we conclude that the origin of the departures is solely due to the choice of method, as the abundances with XIRU-based stellar parameters better follow the GCE trend. Interestingly, the B component, a K-type star, follows the GCE trend of G-type stars, indicating that we can apply our GCE corrections (see below).

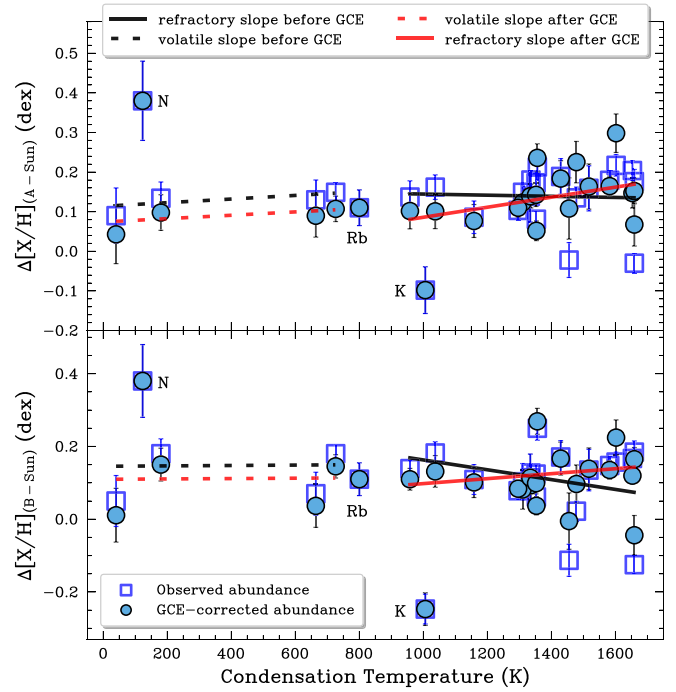


Figure 10. The same as Figure 9, but with abundances estimated using ISOCHRONES-based stellar parameters.

In order to accurately compare the pair with the Sun, it is necessary to consider the GCE of stars. Comprehensive studies such as those of Nissen (2015), Bedell et al. (2018), and Spina et al. (2018) have provided crucial insights into GCE in the solar neighborhood. These studies established GCE trends for solar twin stars by fitting individual abundances and ages, while also accounting for [Fe/H] effects. In this study, we use our updated GCE corrections, which are based on data from 200 G-type stars (J. Yana Galarza et al. 2024b, in preparation). For all the elements, we fitted the [Fe/H] versus age relation using linear and polynomial models that account for the uncertainties in [Fe/H] and ages. Once we found the parameters that define the best-fitting line and curve, we used these models to correct the abundances of the pair for GCE effects. Since the system is older than the Sun, we removed the GCE effects. We refer to Bedell et al. (2014), Yana Galarza et al. (2016b), and Spina et al. (2016) for more details.

In Figure 9 (XIRU-based stellar parameters) and Figure 10 (ISOCHRONES-based stellar parameters), the differential abundances of star A (upper panel) and B (bottom panel) relative to the Sun in the condensation temperature (taken from the 50% condensation temperature values inferred by Lodders 2003) plane is shown. We consider the volatile elements to have $T_C < 900$ K, while refractory elements have $T_C > 900$ K, as stated in Meléndez et al. (2009).

The linear fits were carried out using the Fitter object of the KAPTEYN kmfpt package, which takes into account abundance uncertainties. The slopes of the fits for the refractory elements in components A and B before and after GCE correction are listed in Table 7.

From Figures 9 and 10, it is clear that the T_C slopes for volatile elements, both before and after GCE corrections, are not statistically significant, indicating that both components exhibit similar abundance patterns to the Sun. The only statistically significant T_C slope observed for the refractory

Table 6
Chemical Abundances Relative to the Sun for the Wide Binary system TOI-1173 A/B

Element	Z	TOI-1173 A ^a $\Delta[X/H]$ (dex)	TOI-1173 B ^a $\Delta[X/H]$ (dex)	TOI-1173 A ^c $\Delta[X/H]$ (dex)	TOI-1173 B ^c $\Delta[X/H]$ (dex)
C I	6	0.100 ± 0.080	0.060 ± 0.080	0.090 ± 0.070	0.050 ± 0.100
N I	7	0.340 ± 0.100	0.330 ± 0.100	0.380 ± 0.100	0.370 ± 0.110
O I ^b	8	0.185 ± 0.016	0.180 ± 0.034	0.134 ± 0.041	0.180 ± 0.050
Na I	11	0.137 ± 0.031	0.149 ± 0.049	0.137 ± 0.041	0.139 ± 0.061
Mg I	12	0.191 ± 0.016	0.153 ± 0.028	0.180 ± 0.022	0.127 ± 0.029
Al I	13	0.208 ± 0.022	0.182 ± 0.027	0.204 ± 0.025	0.167 ± 0.033
Si I	14	0.167 ± 0.012	0.125 ± 0.019	0.149 ± 0.016	0.103 ± 0.025
S I	16	0.110 ± 0.030	0.082 ± 0.044	0.130 ± 0.050	0.070 ± 0.080
K I	19	−0.086 ± 0.029	−0.238 ± 0.025	−0.098 ± 0.029	−0.247 ± 0.025
Ca I	20	0.112 ± 0.024	0.110 ± 0.048	0.159 ± 0.057	0.135 ± 0.053
Sc I	21	0.189 ± 0.051	0.200 ± 0.056	0.198 ± 0.055	0.200 ± 0.048
Sc II	21	0.224 ± 0.022	0.196 ± 0.047	0.166 ± 0.037	0.176 ± 0.035
Ti I	22	0.170 ± 0.018	0.180 ± 0.033	0.192 ± 0.043	0.142 ± 0.046
Ti II	22	0.160 ± 0.036	0.150 ± 0.043	0.173 ± 0.030	0.151 ± 0.036
V I	23	0.184 ± 0.014	0.180 ± 0.041	0.189 ± 0.045	0.171 ± 0.054
Cr I	24	0.158 ± 0.012	0.105 ± 0.023	0.100 ± 0.029	0.060 ± 0.035
Cr II	24	0.140 ± 0.025	0.110 ± 0.080	0.110 ± 0.041	0.110 ± 0.046
Mn I	25	0.108 ± 0.025	0.069 ± 0.035	0.086 ± 0.041	0.109 ± 0.080
Fe ^d	26	0.126 ± 0.010	0.107 ± 0.020	0.139 ± 0.065	0.114 ± 0.069
Co I	27	0.164 ± 0.014	0.112 ± 0.026	0.173 ± 0.025	0.124 ± 0.025
Ni I	28	0.129 ± 0.020	0.098 ± 0.023	0.081 ± 0.020	0.061 ± 0.035
Cu I	29	0.202 ± 0.020	0.209 ± 0.062	0.162 ± 0.031	0.182 ± 0.054
Zn I	30	0.194 ± 0.029	0.206 ± 0.025	0.149 ± 0.024	0.180 ± 0.060
Rb I	37	0.110 ± 0.045	0.100 ± 0.045	0.110 ± 0.045	0.090 ± 0.035
Y II	39	0.081 ± 0.035	−0.006 ± 0.040	−0.030 ± 0.024	−0.125 ± 0.027
Ba II	56	0.092 ± 0.025	0.040 ± 0.035	−0.022 ± 0.044	−0.113 ± 0.054
Ce II	58	0.142 ± 0.027	0.020 ± 0.019	0.135 ± 0.027	0.022 ± 0.020
Nd II	60	0.230 ± 0.022	0.160 ± 0.042	0.217 ± 0.027	0.157 ± 0.032
Eu II	63	0.208 ± 0.033	0.221 ± 0.020	0.213 ± 0.033	0.250 ± 0.024

Notes.^a Differential abundances relative to the Sun using XIRU-based stellar parameters.^b Oxygen NLTE-corrected abundances using the grades of Ramírez et al. (2007).^c Differential abundances relative to the Sun using ISOCHRONES-based stellar parameters.^d Weighted average of Fe I and Fe II.**Table 7**

Slopes Derived from Linear Fits to Refractory Elements Before and After GCE Corrections

Category	Slope (dex K ^{−1})	Method
Before GCE corrections		
Refractory (A-Sun)	$0.529(\pm 0.265) \times 10^{-4}$	XIRU
Refractory (B-Sun)	$-0.013(\pm 0.440) \times 10^{-4}$	XIRU
Refractory (A-Sun)	$-0.142(\pm 0.359) \times 10^{-4}$	ISOCHRONES
Refractory (B-Sun)	$-1.351(\pm 0.469) \times 10^{-4}$	ISOCHRONES
After GCE corrections		
Refractory (A-Sun)	$1.125(\pm 0.303) \times 10^{-4}$	XIRU
Refractory (B-Sun)	$1.061(\pm 0.512) \times 10^{-4}$	XIRU
Refractory (A-Sun)	$1.267(\pm 0.466) \times 10^{-4}$	ISOCHRONES
Refractory (B-Sun)	$0.682(\pm 0.613) \times 10^{-4}$	ISOCHRONES




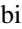
elements is the A component after GCE corrections, although at a marginal significance level of 2.7σ . Thus, we conclude that both components exhibit abundance patterns similar to the Sun after being corrected for GCE effects. It is worth highlighting that N I and K I elements are excluded from our fits, because

they are anomalous compared to the Sun and do not follow the volatile/refractory abundance trend observed in both stars. Additionally, although Rb I follows the volatile trend for our pair, we exclude it from our fits, as no GCE correction is available.

Discrepancies of some elements are the typical challenge faced in differential analysis when the target and the reference star do not have similar enough stellar parameters. In that case, uncertainties arising from atmospheric models and NLTE effects are not minimized, thus affecting the precision of the comparison and potentially obscuring signatures of planet formation or engulfment. Here, a differential analysis between the components is the most appropriate approach, given the modest temperature difference between the two stars.

ORCID iDs

Jhon Yana Galarza  <https://orcid.org/0000-0001-9261-8366>
 Henrique Reggiani  <https://orcid.org/0000-0001-6533-6179>
 Thiago Ferreira  <https://orcid.org/0000-0003-2059-470X>
 Diego Lorenzo-Oliveira  <https://orcid.org/0000-0002-1387-2954>
 Joshua D. Simon  <https://orcid.org/0000-0002-4733-4994>
 Andrew McWilliam  <https://orcid.org/0000-0002-0765-431X>

Kevin C. Schlafman  <https://orcid.org/0000-0001-5761-6779>
 Paula Miquelarena  <https://orcid.org/0000-0002-5077-5774>
 Matias Flores Trivigno  <https://orcid.org/0000-0003-4749-8486>
 Marcelo Jaque Arancibia  <https://orcid.org/0000-0002-8086-5746>

References

- Adibekyan, V. Z., González Hernández, J. I., Delgado Mena, E., et al. 2014, *A&A*, **564**, L15
- Adibekyan, V. Z., Sousa, S. G., Santos, N. C., et al. 2012, *A&A*, **545**, A32
- Alencastro Puls, A. 2023, PhD thesis, Australian National Univ.
- Arenou, F., Luri, X., Babusiaux, C., et al. 2018, *A&A*, **616**, A17
- Armstrong, D. J., Lopez, T. A., Adibekyan, V., et al. 2020, *Natur*, **583**, 39
- Asplund, M., Amarsi, A. M., & Grevesse, N. 2021, *A&A*, **653**, A141
- Astropy Collaboration, Price-Whelan, A. M., Lim, P. L., et al. 2022, *ApJ*, **935**, 167
- Bailer-Jones, C. A. L., Rybizki, J., Fousneau, M., Demleitner, M., & Andrae, R. 2021, *AJ*, **161**, 147
- Bayo, A., Rodrigo, C., Barrado Y Navascués, D., et al. 2008, *A&A*, **492**, 277
- Bedell, M., Bean, J. L., Meléndez, J., et al. 2018, *ApJ*, **865**, 68
- Bedell, M., Meléndez, J., Bean, J. L., et al. 2014, *ApJ*, **795**, 23
- Behrman, A., Dai, F., Brewer, J. M., Berger, T. A., & Howard, A. W. 2023, *MNRAS*, **521**, 2969
- Bensby, T., Feltzing, S., & Oey, M. S. 2014, *A&A*, **562**, A71
- Bhatti, W., Bouma, L., Bhatti, et al. 2021, waqasbhatti/astrobase: astrobase v0.5.3, Zenodo, doi:10.5281/zenodo.4445344
- Biazzo, K., Gratton, R., Desidera, S., et al. 2015, *A&A*, **583**, A135
- Blackwell-Whitehead, R. J., Pickering, J. C., Pearse, O., & Nave, G. 2005a, *ApJS*, **157**, 402
- Blackwell-Whitehead, R. J., Toner, A., Hibbert, A., Webb, J., & Ivarsson, S. 2005b, *MNRAS*, **364**, 705
- Blanco-Cuaresma, S. 2019, *MNRAS*, **486**, 2075
- Blanco-Cuaresma, S., Soubiran, C., Heiter, U., & Jofré, P. 2014, *A&A*, **569**, A111
- Booth, R. A., & Owen, J. E. 2020, *MNRAS*, **493**, 5079
- Bovy, J. 2015, *ApJS*, **216**, 29
- Brahm, R., Jordán, A., & Espinoza, N. 2017, *PASP*, **129**, 034002
- Broyden, C. G. 1965, *MaCom*, **19**, 577
- Buchner, J., Georgakakis, A., Nandra, K., et al. 2014, *A&A*, **564**, A125
- Capitanio, L., Lallement, R., Vergely, J. L., Elyajouri, M., & Monreal-Ibero, A. 2017, *A&A*, **606**, A65
- Carlos, M., Meléndez, J., Spina, L., et al. 2019, *MNRAS*, **485**, 4052
- Carlos, M., Nissen, P. E., & Meléndez, J. 2016, *A&A*, **587**, A100
- Casagrande, L. 2018, in IAU Symp. 330, *Astrometry and Astrophysics in the Gaia Sky*, ed. A. Recio-Blanco et al. (Cambridge: Cambridge University Press), 206
- Casagrande, L., Lin, J., Rains, A. D., et al. 2021, *MNRAS*, **507**, 2684
- Castelli, F., & Kurucz, R. L. 2003, in IAU Symp. 210, *Modelling of Stellar Atmospheres*, ed. N. Piskunov, W. W. Weiss, & D. F. Gray (Cambridge: Cambridge Univ. Press), A20
- Chambers, J. E. 2009, *AREPS*, **37**, 321
- Choi, J., Dotter, A., Conroy, C., et al. 2016, *ApJ*, **823**, 102
- Church, R. P., Mustill, A. J., & Liu, F. 2020, *MNRAS*, **491**, 2391
- Cohen, J. G., Christlieb, N., Qian, Y. Z., & Wasserburg, G. J. 2003, *ApJ*, **588**, 1082
- Delgado Mena, E., Israelian, G., González Hernández, J. I., et al. 2014, *A&A*, **562**, A92
- Delgado Mena, E., Tsantaki, M., Adibekyan, V. Z., et al. 2017, *A&A*, **606**, A94
- Demarque, P., Woo, J.-H., Kim, Y.-C., & Yi, S. K. 2004, *ApJS*, **155**, 667
- Dong, J., Huang, C. X., Zhou, G., et al. 2021, *ApJL*, **920**, L16
- Dotter, A. 2016, *ApJS*, **222**, 8
- El-Badry, K., Rix, H.-W., & Heintz, T. M. 2021, *MNRAS*, **506**, 2269
- Evans, D. W., Riello, M., De Angeli, F., et al. 2018, *A&A*, **616**, A4
- Fabrichius, C., Luri, X., Arenou, F., et al. 2021, *A&A*, **649**, A5
- Fabrycky, D., & Tremaine, S. 2007, *ApJ*, **669**, 1298
- Feltzing, S., & Chiba, M. 2013, *NewAR*, **57**, 80
- Feroz, F., & Hobson, M. P. 2008, *MNRAS*, **384**, 449
- Feroz, F., Hobson, M. P., & Bridges, M. 2009, *MNRAS*, **398**, 1601
- Feroz, F., Hobson, M. P., Cameron, E., & Pettitt, A. N. 2019, *OJAp*, **2**, 10
- Flores, M., Yana Galarza, J., Miquelarena, P., et al. 2024, *MNRAS*, **527**, 10016
- Fuhrmann, K., Chini, R., Kaderhandt, L., & Chen, Z. 2017, *MNRAS*, **464**, 2610
- Gaia Collaboration, Brown, A. G. A., Vallenari, A., et al. 2021, *A&A*, **649**, A1
- Gaia Collaboration, Vallenari, A., Brown, A. G. A., et al. 2023, *A&A*, **674**, A1
- Ginsburg, A., Sipőcz, B. M., Brasseur, C. E., et al. 2019, *AJ*, **157**, 98
- González Hernández, J. I., Israelian, G., Santos, N. C., et al. 2010, *ApJ*, **720**, 1592
- Gray, R. O., & Corbally, C. J. 2009, *Stellar Spectral Classification* (Princeton, NJ: Princeton Univ. Press)
- Grievies, N., Ge, J., Thomas, N., et al. 2018, *MNRAS*, **481**, 3244
- Gustafsson, B. 2018a, *A&A*, **616**, A91
- Gustafsson, B. 2018b, *A&A*, **620**, A53
- Hambly, N. C., Cropper, M., Boudreault, S., et al. 2018, *A&A*, **616**, A15
- Hawkins, K., Lucey, M., Ting, Y.-S., et al. 2020, *MNRAS*, **492**, 1164
- Hernquist, L. 1990, *ApJ*, **356**, 359
- Hühn, L. A., & Bitsch, B. 2023, *A&A*, **676**, A87
- Hunter, J. D. 2007, *CSE*, **9**, 90
- Jofré, E., Petrucci, R., Maqueo Chew, Y. G., et al. 2021, *AJ*, **162**, 291
- Jofré, P., Heiter, U., & Soubiran, C. 2019, *ARA&A*, **57**, 571
- Kamdar, H., Conroy, C., Ting, Y.-S., et al. 2019, *ApJ*, **884**, 173
- Kervella, P., Arenou, F., & Thévenin, F. 2022, *A&A*, **657**, A7
- Kharchenko, N. V. 2001, *KFNT*, **17**, 409
- Klose, J. Z., Fuhr, J. R., & Wiese, W. L. 2002, *JPCRD*, **31**, 217
- Lallement, R., Capitanio, L., Ruiz-Dern, L., et al. 2018, *A&A*, **616**, A132
- Lallement, R., Vergely, J. L., Valette, B., et al. 2014, *A&A*, **561**, A91
- Lawler, J. E., Wood, M. P., Den Hartog, E. A., et al. 2014, *ApJS*, **215**, 20
- Li, J. 2023, AstroJacobLi/smplotlib: v0.0.9, Zenodo, doi:10.5281/zenodo.8126529
- Lind, K., Asplund, M., & Barklem, P. S. 2009, *A&A*, **503**, 541
- Lindgren, L., Bastian, U., Biermann, M., et al. 2021a, *A&A*, **649**, A4
- Lindgren, L., Klioner, S. A., Hernández, J., et al. 2021b, *A&A*, **649**, A2
- Liu, F., Asplund, M., Ramirez, I., Yong, D., & Melendez, J. 2014, *MNRAS*, **442**, L51
- Liu, F., Bitsch, B., Asplund, M., et al. 2021, *MNRAS*, **508**, 1227
- Liu, F., Ting, Y.-S., Yong, D., et al. 2024, *Natur*, **627**, 501
- Liu, F., Yong, D., Asplund, M., et al. 2018, *A&A*, **614**, A138
- Lodders, K. 2003, *ApJ*, **591**, 1220
- Lorenzo-Oliveira, D., Meléndez, J., Yana Galarza, J., et al. 2019, *MNRAS*, **485**, L68
- Mack, C. E. I., Schuler, S. C., Stassun, K. G., & Norris, J. 2014, *ApJ*, **787**, 98
- Maia, M. T., Meléndez, J., Lorenzo-Oliveira, D., Spina, L., & Jofré, P. 2019, *A&A*, **628**, A126
- Mardling, R. A., & Lin, D. N. C. 2004, *ApJ*, **614**, 955
- Martos, G., Meléndez, J., Rathsam, A., & Carvalho Silva, G. 2023, *MNRAS*, **522**, 3217
- McKinney, W. 2010, in Proc. of the 9th Python in Science Conf., ed. S. van der Walt & J. Millman, 51
- McWilliam, A. 1998, *AJ*, **115**, 1640
- Meléndez, J., Asplund, M., Gustafsson, B., & Yong, D. 2009, *ApJL*, **704**, L66
- Meléndez, J., Bedell, M., Bean, J. L., et al. 2017, *A&A*, **597**, A34
- Meléndez, J., Dodds-Eden, K., & Robles, J. A. 2006, *ApJL*, **641**, L133
- Meléndez, J., Ramírez, I., Karakas, A. I., et al. 2014, *ApJ*, **791**, 14
- Michaud, G., Fontaine, G., & Beaudet, G. 1984, *ApJ*, **282**, 206
- Miquelarena, P., Saffe, C., Flores, M., et al. 2024, *A&A*, **688**, A73
- Miyamoto, M., & Nagai, R. 1975, *PASJ*, **27**, 533
- Mortier, A., Santos, N. C., Sousa, S. G., et al. 2013, *A&A*, **558**, A106
- Morton, T. D., 2015 isochrones: Stellar model grid package, Astrophysics Source Code Library, ascl:1503.010
- Mugrauer, M., Ginski, C., & Seeliger, M. 2014, *MNRAS*, **439**, 1063
- Mustill, A. J., Davies, M. B., & Johansen, A. 2015, *ApJ*, **808**, 14
- Naoz, S., Farr, W. M., & Rasio, F. A. 2012, *ApJL*, **754**, L36
- Navarro, J. F., Frenk, C. S., & White, S. D. M. 1996, *ApJ*, **462**, 563
- Nelson, T., Ting, Y.-S., Hawkins, K., et al. 2021, *ApJ*, **921**, 118
- Nissen, P. E. 2015, *A&A*, **579**, A52
- Nissen, P. E., & Gustafsson, B. 2018, *A&ARv*, **26**, 6
- Ochsenbein, F., Bauer, P., & Marcout, J. 2000, *A&AS*, **143**, 23
- Oh, S., Price-Whelan, A. M., Brewer, J. M., et al. 2018, *ApJ*, **854**, 138
- Paxton, B., Bildsten, L., Dotter, A., et al. 2011, *ApJS*, **192**, 3
- Paxton, B., Cantiello, M., Arras, P., et al. 2013, *ApJS*, **208**, 4
- Paxton, B., Marchant, P., Schwab, J., et al. 2015, *ApJS*, **220**, 15
- Paxton, B., Schwab, J., Bauer, E. B., et al. 2018, *ApJS*, **234**, 34
- Paxton, B., Smolec, R., Schwab, J., et al. 2019, *ApJS*, **243**, 10
- Placco, V. M., Sneden, C., Roederer, I. U., et al. 2021, *RNAAS*, **5**, 92
- Price-Whelan, A., Sipőcz, B., Lenz, D., et al. 2020, adm/gala: v1.3, Zenodo, doi:10.5281/zenodo.4159870
- Price-Whelan, A. M. 2017, *JOSS*, **388**, 2
- Prochaska, J. X., & McWilliam, A. 2000, *ApJL*, **537**, L57
- Prochaska, J. X., Naumov, S. O., Carney, B. W., McWilliam, A., & Wolfe, A. M. 2000, *AJ*, **120**, 2513
- Ramírez, I., & Allende Prieto, C. 2011, *ApJ*, **743**, 135

- Ramírez, I., Allende Prieto, C., & Lambert, D. L. 2007, *A&A*, **465**, 271
- Ramírez, I., Khanal, S., Aleo, P., et al. 2015, *ApJ*, **808**, 13
- Ramírez, I., Khanal, S., Lichon, S. J., et al. 2019, *MNRAS*, **490**, 2448
- Ramírez, I., Meléndez, J., & Asplund, M. 2009, *A&A*, **508**, L17
- Ramírez, I., Meléndez, J., Bean, J., et al. 2014, *A&A*, **572**, A48
- Ramírez, I., Meléndez, J., Cornejo, D., Roederer, I. U., & Fish, J. R. 2011, *ApJ*, **740**, 76
- Rasio, F. A., & Ford, E. B. 1996, *Sci*, **274**, 954
- Rathsam, A., Meléndez, J., & Carvalho Silva, G. 2023, *MNRAS*, **525**, 4642
- Raymond, S. N., Barnes, R., & Mandell, A. M. 2008, *MNRAS*, **384**, 663
- Reggiani, H., Amarsi, A. M., Lind, K., et al. 2019, *A&A*, **627**, A177
- Reggiani, H., & Meléndez, J. 2017, *CaJPh*, **95**, 855
- Reggiani, H., Schlaufman, K. C., Healy, B. F., Lothringer, J. D., & Sing, D. K. 2022, *AJ*, **163**, 159
- Rice, M., Wang, S., Gerbig, K., et al. 2023, *AJ*, **165**, 65
- Saffe, C., Flores, M., & Buccino, A. 2015, *A&A*, **582**, A17
- Saffe, C., Jofré, E., Martioli, E., et al. 2017, *A&A*, **604**, L4
- Saffe, C., Jofré, E., Miquelarena, P., et al. 2019, *A&A*, **625**, A39
- Saffe, C., Miquelarena, P., Alacoria, J., et al. 2024, *A&A*, **682**, L23
- Salpeter, E. E. 1955, *ApJ*, **121**, 161
- Schönrich, R. 2012, *MNRAS*, **427**, 274
- Schönrich, R., Binney, J., & Dehnen, W. 2010, *MNRAS*, **403**, 1829
- Schuler, S. C., Flateau, D., Cunha, K., et al. 2011, *ApJ*, **732**, 55
- Seifahrt, A., Bean, J. L., Kasper, D., et al. 2022, *Proc. SPIE*, **12184**, 121841G
- Seifahrt, A., Stürmer, J., Bean, J. L., & Schwab, C. 2018, *Proc. SPIE*, **10702**, 107026D
- Sevilla, J., Behrard, A., & Fuller, J. 2022, *MNRAS*, **516**, 3354
- Skrutskie, M. F., Cutri, R. M., Stiening, R., et al. 2006, *AJ*, **131**, 1163
- Smiljanic, R., Porto de Mello, G. F., & da Silva, L. 2007, *A&A*, **468**, 679
- Snedden, C. A. 1973, PhD thesis, Univ. of Texas at Austin
- Speagle, J. S. 2020, *MNRAS*, **493**, 3132
- Spina, L., Meléndez, J., Karakas, A. I., et al. 2016, *A&A*, **593**, A125
- Spina, L., Meléndez, J., Karakas, A. I., et al. 2018, *MNRAS*, **474**, 2580
- Spina, L., Sharma, P., Meléndez, J., et al. 2021, *NatAs*, **5**, 1163
- Terlouw, J. P., & Vogelaar, M. G. R., 2016 Kapteyn Package: Tools for developing astronomical applications, Astrophysics Source Code Library, ascl:1611.010
- Teske, J. K., Ghezzi, L., Cunha, K., et al. 2015, *ApJL*, **801**, L10
- Teske, J. K., Khanal, S., & Ramírez, I. 2016, *ApJ*, **819**, 19
- Tody, D. 1986, *Proc. SPIE*, **627**, 733
- Torra, F., Castañeda, J., Fabricius, C., et al. 2021, *A&A*, **649**, A10
- Tsantaki, M., Sousa, S. G., Santos, N. C., et al. 2014, *A&A*, **570**, A80
- Tucci Maia, M., Meléndez, J., & Ramírez, I. 2014, *ApJL*, **790**, L25
- van der Walt, S., Colbert, S. C., & Varoquaux, G. 2011, *CSE*, **13**, 22
- Wenger, M., Ochsenbein, F., Egret, D., et al. 2000, *A&AS*, **143**, 9
- Wu, Y., & Murray, N. 2003, *ApJ*, **589**, 605
- Yana Galarza, J., Ferreira, T., Lorenzo-Oliveira, D., et al. 2024, *AJ*, **168**, 91
- Yana Galarza, J., López-Valdivia, R., Lorenzo-Oliveira, D., et al. 2021b, *MNRAS*, **504**, 1873
- Yana Galarza, J., López-Valdivia, R., Meléndez, J., & Lorenzo-Oliveira, D. 2021c, *ApJ*, **922**, 129
- Yana Galarza, J., Meléndez, J., & Cohen, J. G. 2016a, *A&A*, **589**, A65
- Yana Galarza, J., Meléndez, J., Karakas, A. I., Asplund, M., & Lorenzo-Oliveira, D. 2021a, *MNRAS*, **502**, L104
- Yana Galarza, J., Meléndez, J., Ramírez, I., et al. 2016b, *A&A*, **589**, A17
- Yi, S., Demarque, P., Kim, Y.-C., et al. 2001, *ApJS*, **136**, 417
- Yong, D., Liu, F., Ting, Y.-S., et al. 2023, *MNRAS*, **526**, 2181
- Zechmeister, M., Reiners, A., Amado, P. J., et al. 2018, *A&A*, **609**, A12